

# An ensemble machine-learning first-guess approach for physics-based retrieval of ice particle size distributions from multi-frequency radar, validated with CCREST-M aircraft observations

Anthony J. Baran<sup>1,2</sup>, Stuart Fox<sup>1</sup>, Richard Cotton<sup>1</sup>, Julien Delanoë<sup>3</sup>, Christopher J. Walden<sup>4,5</sup>, Karina McCusker<sup>6</sup>, Christopher D. Westbrook<sup>6</sup> & Peter G. Huggard<sup>4</sup>

<sup>1</sup>Met Office, FitzRoy Road, Exeter, EX1 3PB, UK

<sup>2</sup>School of Physics, Astronomy, and Mathematics, University of Hertfordshire, Hatfield, AL10 9AB, UK

<sup>3</sup>Laboratoire Atmosphère, Milieux et Observations Spatiales, IPSL, UVSQ Université Paris-Saclay, Sorbonne Université, CNRS, Guyancourt, France

10 <sup>4</sup>RAL Space, STFC Rutherford Appleton Laboratory, Didcot, OX11 0QX, UK

<sup>5</sup>National Centre for Atmospheric Science, Leeds, UK

<sup>6</sup>Department of Meteorology, University of Reading, Reading, UK

*Correspondence to:* Anthony J. Baran (anthony.baran@metoffice.gov.uk)

**Abstract.** The Characterising CiRrus and icE cloud across the spectrum-Microwave (CCREST-M) aircraft campaign (February–March 2024) was based around the Chilbolton Observatory, UK, using the Facility for Airborne Atmospheric Measurements (FAAM) BAe-146 aircraft together with ground-based multi-frequency radars to provide a testbed for ice-cloud scattering and radiative transfer models across the microwave and sub-millimetre spectrum. Ice particle size distributions (PSDs) are retrieved from the ground-based zenith-pointing radars at the time of the radiometric overpasses, and the aircraft in-situ PSDs are used as an independent validation dataset.

20 We present a novel hybrid retrieval framework for mid-latitude ice PSD parameters (slope  $\lambda$ , intercept  $N_0$ , and shape  $\mu$  of the gamma size distribution) that combines a machine-learning (ML) ensemble with physics-based multi-frequency radar retrievals using 3, 35, and 94 GHz reflectivities. An ensemble of ML models is trained on observations from the Parameterising Ice Clouds using Airborne ObservationS and triple-frequency Doppler radar (PICASSO) campaign, also centred on Chilbolton Observatory. These models predict PSD moments from temperature, pressure, 3 GHz-retrieved ice water content (IWC), and the mean mass-weighted dimension. The ML predictions are converted into first guess gamma-PSD parameters at each height. A subsequent deterministic optimisation then adjusts  $N_0$  and  $\lambda$ , using a randomly oriented rosette-aggregate scattering model, to enforce simultaneous agreement with the observed 35 and 94 GHz reflectivities.

30 Application of the above method to three CCREST-M cases show that the ML ensemble reproduces PSD moments well for two cases but fails when extrapolating beyond its trained temperature range in the third case. Retrieved IWCs from the 3 GHz radar compare favourably with in-situ measurements of IWC, and exponential ( $\mu=0$ ) and gamma PSD assumptions show comparable performance overall. Retrieved mean PSDs show generally good agreement with in-situ PSDs as a function of temperature for two of the cases, with IWCs within about 50% of the in-situ measured IWCs over much of the -50 to -10°C

temperature range. The systematic biases seen in one case are attributed to temporal cloud evolution between radar and in-situ sampling. Independent validation using 200 GHz radar reflectivity profiles shows good agreement between the forward-  
35 modelled reflectivities and measurements above about 4.5 km. Below 4.5 km the agreement is more sparse owing to the likely presence of dendritic particles, which depart from the rosette-aggregate scattering assumption.

## 1 Introduction

Accurate representation of ice crystal scattering properties and PSDs in cirrus and ice clouds is fundamental to improving numerical weather prediction and climate modelling (Liou 1986; Baran 2009; Baran, 2012; Yang et al., 2015; Liou and Yang  
40 2016; Krämer et al., 2025), and data assimilation (Geer and Baordo 2014; Geer et al., 2017; Geer 2021). Moreover, satellite missions such as EarthCARE (Earth, Clouds, Aerosols and Radiation Explorer; Illingworth et al. 2015; Mason et al. 2024; Barker et al., 2025) and the forthcoming Ice Cloud Imager (ICI; Eriksson et al., 2020; May et al. 2024) further heighten the need for realistic forward operators linking cloud microphysics to radar and radiometric observables.

The assimilation of radar reflectivity into weather prediction models has become increasingly important for improving  
45 convective precipitation forecasts, as radar reflectivity provides information on the vertical structure of hydrometeors, IWC and on cloud development. However, this requires accurate forward operators that link model state variables to radar observations (Janisková, 2015; Liu et al., 2024), placing stringent demands on ice crystal scattering representations. Earlier work by Baran et al. (2011) demonstrated that ensemble models of ice crystals could be used to simulate equivalent radar reflectivity at 94 GHz with forward model errors generally within  $\pm 2$  dBZ. Subsequent studies have demonstrated that  
50 spheroidal approximations can bias retrieved water contents (Fontaine et al., 2017; Schrom and Kumjian, 2019), and studies that directly assimilate radar reflectivity from both rainwater and ice-phase species (i.e., snow and graupel) have shown that the ice species significantly improves the analysis of the vertical hydrometeor spatial distributions (Wang and Liu, 2019). Moreover, a study by Hong et al. (2025), building on the findings of Baran et al. (2011) and Wu et al. (2024), demonstrated that incorporating multiple ice habits in the retrieval of snowfall rate from passive microwave radiometers significantly  
55 improved retrieval accuracy compared to assuming single ice crystal habits. Polarimetric observations above 100 GHz have suggested that mixtures of random and oriented ice crystals may be needed to represent natural variability within the ice cloud (Brath et al., 2020; McCusker et al., 2024).

A further uncertainty in retrievals of ice cloud properties is the functional form of the PSD. Recent studies have shown contrasting results, with Bartolomé García et al. (2024) suggesting that bimodal PSDs may offer improved realism over  
60 monomodal representations, especially in complex cloud scenes. However, for larger particles—such as those found in snow, where radar reflectivity becomes more sensitive to the upper end of the size distribution—exponential forms are still widely used. For instance, Wood and L’Ecuyer (2021) argue for the adequacy of exponential PSDs in their W-band retrievals of snow properties based on observational evidence. Similarly, McCusker et al. (2024) adopted an exponential PSD assumption to retrieve the slope parameter while holding the intercept parameter fixed, to characterise PSDs in a frontal mid-latitude system

65 using airborne 35 GHz radar measurements. Their retrievals were able to replicate the polarisation dependent brightness  
temperature depressions observed at 243 GHz using the International Sub-Millimetre Airborne Radiometer (ISMAR; Fox et  
al., 2017). Conversely, gamma distributions have been preferred in other studies. For instance, Heymsfield et al. (2023),  
analysing quadruple-frequency radar observations from the Investigation of Microphysics and Precipitation for Atlantic Coast-  
Threatening Snowstorms (IMPACTS) field campaign data, prefer gamma PSDs to characterise snowstorms. Using the same  
70 dataset, Duffy and Posselt (2022) found that a gamma distribution with  $\mu = -1.25$  best represented the mass- and reflectivity-  
related moments of the observed PSDs. These differences highlight the need for retrieval frameworks that can flexibly  
accommodate both exponential and gamma PSDs while remaining physically constrained by realistic scattering models.

Closure tests between ice-cloud scattering models and radiometric observations require a near one-to-one relationship  
between the PSDs used as input to the radiative transfer model and the radiometric measurements. Since a single research  
75 aircraft cannot simultaneously perform above-cloud radiometric measurements and in-situ microphysics sampling within the  
same cloud volume, we must retrieve the PSDs from ground-based multi-frequency radars that are co-incident with the  
radiometric overpasses. The CCREST-M campaign was designed to address this challenge by combining the FAAM BAe-146  
aircraft measurements with co-located ground-based multi-frequency radars. The PSDs are then retrieved from the zenith-  
pointing radars at the same time as the radiometric overpasses, and the in-situ measured PSDs serve as an independent  
80 validation dataset. In this paper, we present a novel retrieval framework that combines an ensemble of machine learning models  
with physical radar retrievals to estimate PSD gamma parameters and IWC from 3, 35 and 94 GHz radar observations. The  
ML ensemble provides first-guess estimates of the PSD parameters from inputs of temperature, pressure, 3 GHz-retrieved IWC  
and the median mass-weighted dimension, where the latter is estimated from a temperature-dependent second order polynomial  
obtained from the PICASSO climatology. A physical optimisation, using the scattering properties of randomly oriented rosette  
85 aggregates, is then used to modify  $\lambda$  and  $N_0$ , with  $\mu$  kept as its first-guess profile values, at each height level so that simulated  
35 and 94 GHz reflectivities match the observed values.

The retrieved PSDs are compared with the in-situ PSDs measured by the FAAM BAe-146 aircraft for three case studies, and  
the retrieval methodology is further evaluated using the G-band 200 GHz radar reflectivity observations from the Chilbolton  
Observatory GRaCE radar (Courtier et al., 2022). The G-band radar has recently been used by McCusker et al. (2025) to  
90 demonstrate the usefulness of such high-frequency radars to directly retrieve the IWC and snow rate of deep frontal mid-  
latitude cloud. This paper is the first demonstration of an ML-ensemble-assisted, physics-based radar retrieval of ice cloud  
PSDs validated with aircraft data. Although the same PICASSO climatology could in principle be used to define Bayesian  
priors in a classical optimal-estimation framework, we instead employ a machine-learning-based first guess. This approach  
implicitly captures the joint distribution of the local climatology without requiring an explicit multivariate error covariance  
95 and vertical correlation structure for  $(N_0, \lambda, \mu)$  and keeps the subsequent physics-based optimisation computationally  
straightforward.

The paper is organised as follows: Section 2 describes the CCREST-M campaign, radars, and aircraft data. Section 3 outlines  
the ice crystal scattering model used in the forward operator, which is also formally defined in this section. Section 4 details

the retrieval methodology, including the ML-ensemble approach developed using the PICASSO dataset, and the optimisation method applied to retrieve the PSD parameters and IWC from the radar reflectivity observations. Section 5 presents the retrieval results for the PSDs using three CCREST-M case studies, with detailed comparisons against in-situ aircraft measurements and forward-modelled radar reflectivities, including their residuals. Section 6 summarises the main findings and provides the conclusions.

## 2 The rationale of the CCREST-M campaign, instrumentation and data

The CCREST-M campaign combined coordinated FAAM BAe-146 aircraft measurements with ground-based radars at the Chilbolton Observatory, UK (51.15° N, 1.44° W; 84 m above mean sea level), to study the microphysical and mm-wave and sub-mm-wave radiative properties of mid-latitude ice clouds. Three radars operated near-synchronously: the 3 GHz CAMRa (Naud et al., 2005), the 35 GHz Kepler, and the 94 GHz mini-BASTA (Delanoë et al., 2016), providing complementary sensitivity across the particle-size spectrum. Detailed specifications for the 35 GHz Kepler radar are provided on the National Centre for Atmospheric Science Atmospheric Measurement and Observation Facility website: <https://amof.ac.uk/instruments/mobile-cloud-radar/>.

This campaign was explicitly designed to deliver multi-frequency active measurements together with near-simultaneous passive measurements extending into the sub-millimetre. In particular, Chilbolton Observatory hosted the multi-frequency radars, and for one of the cases the 200 GHz G-band GRaCE radar, while the FAAM aircraft carried the mm-wave and sub-mm-wave radiometers as well as the in-situ instrumentation. This combination enables the probing of the bulk microphysics with the lower-frequency radars and tests ice crystal scattering and radiative transfer models using the higher frequency radiometers. Since only one aircraft platform was available, CCREST-M could not obtain in-situ microphysical sampling at the same time and location as the radiometric overpasses. High-level radiometric legs and in-situ sampling had to be flown sequentially, so by the time the aircraft descended into the cloud the cloud volume sampled had evolved. In CCREST-M, the strategy is therefore to retrieve the PSDs from the ground-based multi-frequency radars at the time of the radiometric overpasses, and to use the in-situ PSDs from dedicated sampling legs as an independent validation dataset for the retrieved PSDs. This design, with a near one-to-one relationship between the retrieved PSDs and radiometric measurements makes CCREST-M a particularly stringent testbed for ice crystal scattering and radiative transfer models.

The CCREST-M strategy therefore differs from earlier campaigns such as the Cirrus Coupled Cloud-Radiation Experiment (CIRCCREX), the North Atlantic Waveguide and Downstream Impact Experiment (NAWDEX), and PIKNMIX-F, which have provided useful active and/or passive observations of ice cloud but suffered from inexact passive/active collocation or lacked in-situ observations. CCREST-M also builds upon the PICASSO campaign (Sephton, 2022), which collected in-situ bulk and microphysical properties of ice clouds using the FAAM BAe-146 aircraft, alongside co-located ground-based radar observations at 3, 35 and 94 GHz from Chilbolton Observatory, but lacked radiometric mm-wave and sub-mm-wave measurements to complement the multi-frequency radar measurements.

CCREST-M took place between the 6<sup>th</sup> of February and 25<sup>th</sup> of March 2024. Twelve science flights were conducted, three of which — C374 (28<sup>th</sup> February), C379 (19<sup>th</sup> March), and C382 (25<sup>th</sup> March) — included in-situ sampling of the bulk and microphysical properties of the cloud. The duration of each science flight was approximately 4 h and each followed a common flight pattern designed to link the ground-based radars and the radiometers in a repeatable way. Figure 1 shows a typical flight pattern; these consisted of straight and level runs along a radial (270° or 246°) to and from the Chilbolton-based radars, followed by figure-of-eight patterns centred on the Chilbolton Observatory. The decision on which radial to fly along was made in real time as the aircraft approached the Chilbolton area, in coordination with the radar operator. Range Height-Indicator (RHI) scans from mainly the 3 GHz CAMRa radar were used to identify the azimuth containing the deepest and most strongly reflecting ice cloud to ensure a good radiometric signal, and this information was augmented by 15-min 10 μm geostationary satellite imagery. During the radial legs the ground-based radars operated in RHI scanning mode, providing vertical profiles of cloud structure along the aircraft's flight path for radiometer sampling. During the figure-of-eight patterns the aircraft repeatedly flew over the Observatory while the radars were zenith pointing, yielding time–height reflectivity profiles directly beneath the aircraft, while the radiometers sampled the cloud in nadir pointing mode. During the high-level radiometric runs there were dropsonde releases from the aircraft above the cloud to obtain pressure and temperature profiles for use in the retrieval of the PSDs.

After the high-level radiometric overpasses and figure-of-eight loiter, the aircraft descended into the cloud for in-situ microphysics and bulk IWC sampling. For C379 and C382 this took the form of stepped descents with straight-and-level runs of several minutes at successive levels, whereas for C374 the aircraft performed a continuous profiling descent through the depth of the cloud. In all three cases, these in-situ legs act as an independent validation data set for the retrieved PSDs, although they are not strictly co-located with the ground-based radar observations.

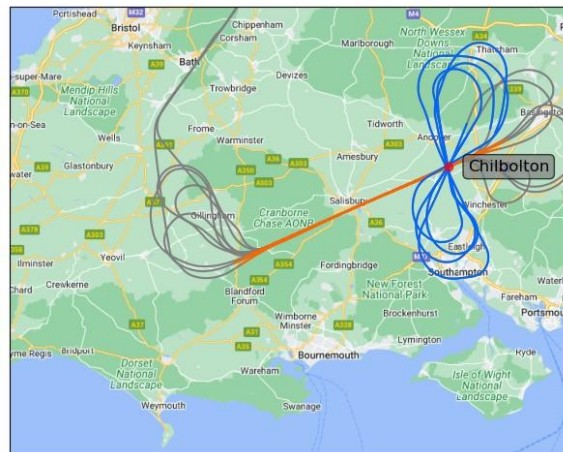


**Figure 1** A typical CCREST-M flight track (shown as the grey, orange and blue colours) towards and over the Chilbolton-based triple-frequency radars. The figure-of-eight patterns (blue) were flown over Chilbolton when all the radars were pointing at zenith. The aircraft flew along a specific flight path, known as the Chilbolton radial (orange), which is set at an angle of 246° or 270°.

## 2.1 Aircraft instrumentation, data summary, in-situ cases and ice crystal habit descriptions

The instrumentation on board the FAAM aircraft that is utilised in this paper is summarised below in Table 1. All the aircraft FAAM data listed in Table 1 is available on the Centre for Environmental Data Analysis (CEDA) website given here: <https://www.ceda.ac.uk/>. For a description of the microphysics and bulk probes shown in Table 1, the CIP-15, CIP-100 and the Nevzorov probe see McFarquhar et al. (2017) and Cotton et al. (2013), respectively. For each flight, the in-situ measurements are composited from the CIP-15 and CIP-100 instruments following Cotton et al. (2013), yielding size distributions from approximately 15  $\mu\text{m}$  to 6.4 mm. The microphysics data processing done here is not different to that applied to the PICASSO campaign. However, here ice crystals smaller than 100  $\mu\text{m}$  were omitted since they contribute negligibly to radar reflectivity and brightness temperature depressions at mm-wave and sub-mm-wave frequencies as shown by McCusker et al. (2024). Some PSDs were excluded if the Nevzorov probe measured IWCs below 0.002  $\text{gm}^{-3}$ , which is the estimated sensitivity of the Nevzorov probe as determined by Abel et al. (2014). Probe shattering effects were minimised through modified inlet arms of the CIP probes and inter-arrival time filtering when compositing the PSDs.

**Table 1** A summary of instrumentation on board the FAAM aircraft during the CCREST-M flights.

Instrument	Measurement
CIP-15	PSD 15 $\mu\text{m}$ – 960 $\mu\text{m}$
CIP-100	PSD 100 $\mu\text{m}$ – 6.4 mm
Nevzorov probe	Bulk ice liquid and water
Drosondes – profiles	Temperature and pressure

In this paper, the roles of the aircraft measurements are as follows. The composite in-situ PSDs are used as a validation dataset for the PSDs retrieved from the multi-frequency radars. The Nevzorov probe provides bulk IWC, which we compare directly to the IWCs derived from the retrieved PSDs. The dropsonde profiles provide temperature and pressure, which are both used as inputs to the machine-learning first-guess, together with the 3 GHz-retrieved IWC and mean mass-weighted dimension. Typically, two to four dropsondes were released from the aircraft above the cloud tops during each case, while the aircraft flew along one of the Chilbolton radials.

### 2.1.1 A data summary of the radar and atmospheric data

The processing of the radar data used here was done by the Chilbolton Observatory staff for the CAMRa and Kepler radar data. The CAMRa and Kepler radar data used in this paper are also available on the CEDA website referenced above. The mini-BASTA and 200 GHz GRaCE radar data were processed by the Laboratoire Atmosphère, Milieux, Observations, Spatiales (LATMOS) and the University of Reading, respectively. During the CCREST-M campaign, the radar measurements coincided with near-direct FAAM aircraft overpasses. The CAMRa, Kepler and mini-BASTA radars were operated in either zenith mode or Range-Height Indicator (RHI) scan mode during the aircraft overpass. The core overpass dataset was constructed from figure-of-eight aircraft flight patterns, with the radars pointing vertically, and extended datasets which includes the RHI scans. In this paper, we consider only the zenith-pointing radar data.

The data from the three main radars (CAMRa, Kepler and mini-BASTA) were interpolated to a common 25 m grid extending to an altitude of 13 km, matching the resolution of the Kepler radar. Reflectivity, Doppler velocity, and spectral width were extracted from each radar system, with signal quality control based on native instrument masks and angular thresholds (e.g. within  $0.1^\circ$  for Kepler,  $0.4^\circ$  for mini-BASTA) to exclude off-zenith and edge-of-beam artefacts. To characterise the radar reflectivity statistics for each of the case studies, the mean, median and the standard deviation were computed within a 40-second window ( $\pm 20$  s) centred on the aircraft nadir time for each of the radar frequencies. In the context of this study, these processed time–height fields provide the reflectivity profiles from which we retrieve the PSDs at the times of the aircraft radiometric overpasses for forthcoming radiative transfer studies that will be presented in a later paper. The 40 s window is a pragmatic choice that balances the need for enough radar samples to obtain robust statistics and to accommodate small timing differences between aircraft and radar data. In a few instances where no valid radar profiles were available during the 40 s window, we instead use the nearest available profiles in time, selected by visual inspection to ensure that the reflectivity structure was sufficiently similar to that during the overpass, and we only retained profiles with valid in-cloud returns.

Atmospheric temperature, pressure, humidity, and ozone profiles were provided using a combination of Vaisala RD41 dropsondes (for altitudes below aircraft level) and a mid-latitude winter climatology (for levels above the aircraft and ozone). Temperature and pressure were linearly interpolated onto the radar grid, and relative humidity was computed with respect to liquid or ice depending on the ambient temperature.

To account for liquid water cloud attenuation, cloud liquid water path (LWP) was retrieved from the Chilbolton HATPRO microwave radiometer (Walden, 2026a), with missing data interpolated over short time gaps. The HATPRO LWP provides a column integrated value and does not constrain the vertical distribution of liquid water. We therefore assume the liquid cloud to be a single layer, with a representative in-cloud temperature taken from the interpolated atmospheric profile, where the cloud top height was manually defined using the ceilometer (Walden, 2026b), lidar, and radar backscatter profiles. The specific liquid water absorption at each radar frequency was computed from the Ellison (2007) absorption model at this representative temperature and multiplied by the HATPRO LWP to give the one-way attenuation. Two-way attenuation by ice crystals at 35 and 94 GHz is not accounted for in this paper. It was previously found by McCusker et al. (2024) that for

similar frontal iced-cloud conditions the two-way path integrated ice attenuation at these frequencies to be well below 1 dBZ. This is consistent with the recent multi-campaign comparison by Li et al. (2026), who reported a median W-band path-integrated snow attenuation of 0.3 dB and a sub-dB spread between parametrisations. Therefore, ice attenuation is not corrected for explicitly in this paper. To account for gaseous attenuation by oxygen and water vapour on the radar

215 reflectivities at 35 and 94 GHz, we computed the two-way partial-column gaseous attenuation from near-surface to each in-cloud retrieval gate using the aircraft dropsonde-derived profiles of temperature, pressure and water vapour volume mixing ratio released near the Chilbolton Observatory. A simplified gas absorption parametrisation was used, consisting of pressure-scaled oxygen absorption and humidity-scaled water vapour absorption, with coefficients providing representative specific attenuation values of 0.02, and 0.1 dB/km for oxygen, and 0.01, and 0.08 dB/km for water vapour at 35 and 94 GHz,

220 respectively, under standard atmospheric conditions as recommended by ITU-R P676.13 (2022). The mean partial-column two-way attenuation at 94 GHz reaches approximately 1.5 dB at 94 GHz for C374, this is consistent with Hogan et al. (2000), who using co-located 35 and 94 GHz radars at Chilbolton Observatory reported a two-way gaseous attenuation at 94 GHz of approximately 2 dB from near-surface to 10 km. At 3 GHz, gaseous attenuation is negligible (specific attenuation values of order 0.001 dB/km for oxygen and zero for water vapour) and is not considered further.

225 This dataset enables the construction of well-collocated multi-frequency radar reflectivity profiles, corrected for atmospheric and liquid water attenuation, with matched atmospheric profiles needed for the retrievals and radiative transfer. Here, we utilise only the mean radar reflectivity radar profiles.

### 2.1.2 Case summaries and predominant ice crystal habits

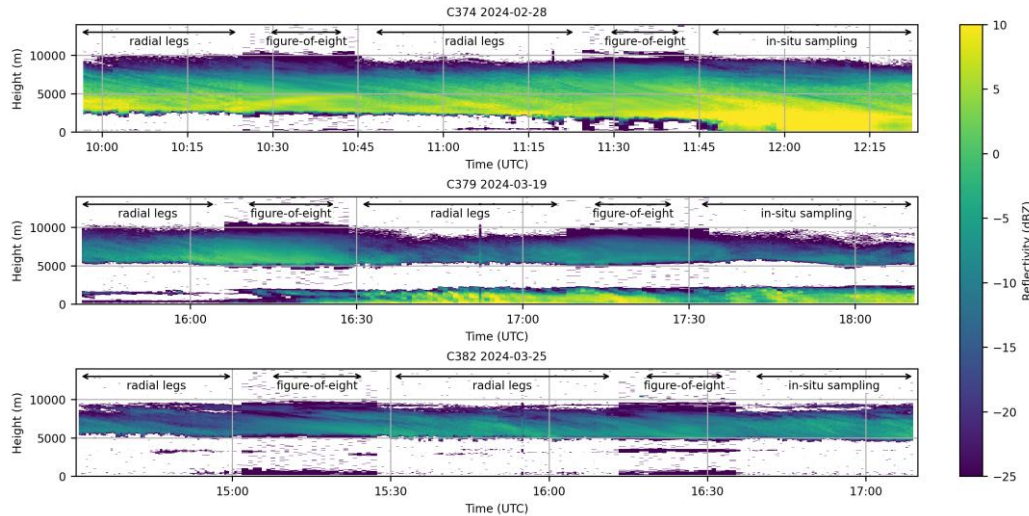
The synoptic environments of the three flights were typical of winter mid-latitude frontal systems over the UK, with non-

230 precipitating cloud during the science flying for C374 and weakly precipitating ice clouds during the science flying for C379 and C382. Figure 2 summarises the temporal and vertical structure of the three CCREST-M cases using time–height plots of 35 GHz Kepler radar reflectivity. For C374 (Fig. 2, top panel), a deep frontal ice cloud is observed, with radar reflectivities ranging from approximately +10 to -25 dBZ between about 3 to 9 km for over two hours. Above about 9 km, the radar detects weaker and more intermittent returns, consistent with sparse upper-level ice cloud. Scientific flying for this case concluded at

235 around 11:45 UTC as significant precipitation began. For C379 (Fig. 2, middle panel), the primary ice layer is located between about 5 and 9 km. Below about 2 km, stronger and more variable reflectivities indicate the presence of an underlying liquid water cloud, which occasionally produced light precipitation of around 1 mm/hr at the surface, as recorded by the Observatory rain gauges. The C382 (Fig. 2, bottom panel) case exhibits a somewhat generally thinner main ice layer than in the other cases, extending from roughly 5 to 8 km. A shallow cirrus layer is present just below approximately 9 km, with a thickness of less

240 than 1 km, and occasional low level-level liquid water cloud is also detected by the Kepler radar. For the cases C374 and C382, the liquid water paths were typically below 0.2 g m<sup>-2</sup>. Overall, these time–height cross-sections confirm that all three cases

correspond to mid-latitude frontal ice cloud with relatively persistent vertical structure, making them well suited for the radiometric overpasses and radar-based PSD retrievals.



245 **Figure 2** Time–height cross-sections of 35 GHz Kepler radar reflectivity for the three CCREST-M cases: C374 (2024-02-28, top panel), C379 (2024-03-19, middle panel), and C382 (2024-03-25, bottom panel). Colours show the radar reflectivity (dBZ) at the native time–height resolution of the complete (i.e., RHI and Zenith-pointing data) processed Kepler dataset, with white areas indicating the absence of cloud or values below the noise threshold. The time periods used for the aircraft radial legs, figure-of-eight manoeuvres, and in-situ sampling are indicated at the top of each panel. The 35 GHz radar is shown here as it provides a good compromise between sensitivity to ice crystals and susceptibility to attenuation. The colour bar on the right-hand side provides the radar reflectivity scale.

250

The most detailed analysis of C374 has already been reported by McCusker et al. (2025), who also provide a detailed description of the observed ice crystal habits for that case. Consistent with that study, examination of CIP-15 imagery from all three flights shows rosettes and aggregates of rosettes as the dominant particle types, with occasional columns, plates, and aggregates of columns. Typical examples of the CIP-15 imagery from the three cases are presented in Fig. 3 (a – c), where the image files were manually examined to identify the predominant ice crystal shapes across different altitudes, and the imagery is taken from the mid-point of each profile. Across all the three cases, a similar vertical evolution of ice crystal habit was observed as shown in the figure. That is, near cloud top the habits consisted of small, pristine rosettes and some columns. At mid-level in the cloud, larger more complex rosette aggregates were observed and at near cloud base, extensive irregular rosette aggregates and occasional columns and column aggregates were observed.

255

260

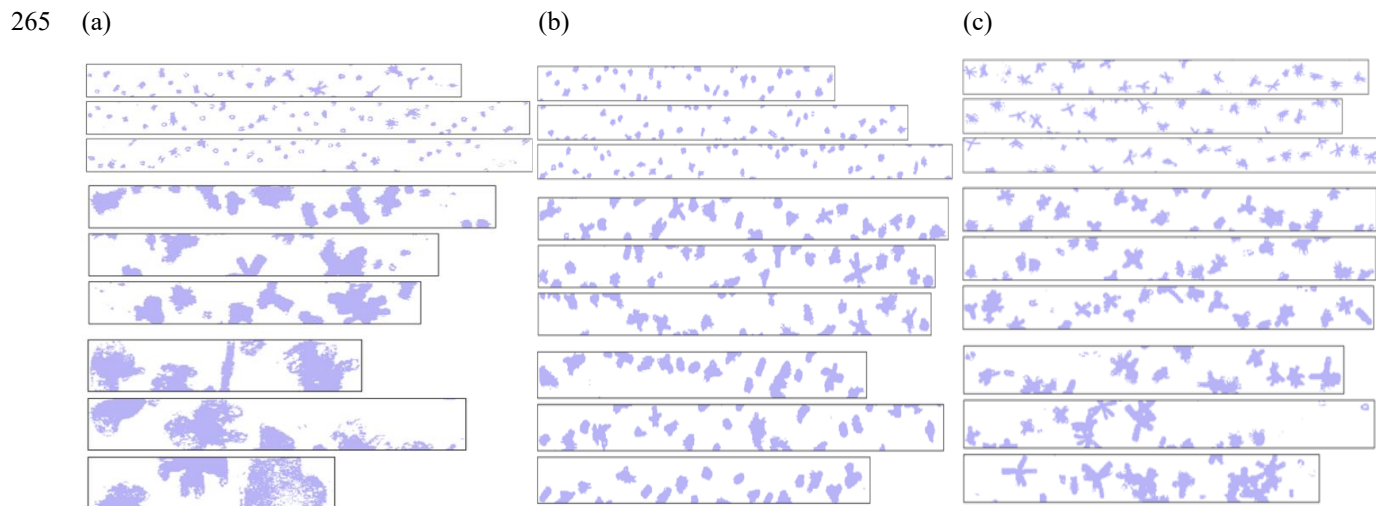


**Figure 3** Representative CIP-15 imagery obtained during three distinct altitude levels. In each panel, the top three rectangular strips correspond to cloud top, followed by the next three representing the cloud mid-level, and the bottom three rectangular strips represent the cloud base during descent through the ice layer for cases (a) C374, (b) C379, and (c) C382. Each rectangular strip spans 64 pixels across the CIP-15 array, corresponding to a physical width of 960  $\mu\text{m}$  at 15  $\mu\text{m}$  per pixel. The length of each strip is variable.

275 Although the three ice cloud cases differ in altitude and temperature, their microphysical ice crystal shape characteristics were broadly consistent, making them ideal cases for testing the retrieval methodology under comparable mid-latitude conditions. The same rosette-aggregate habits observed here underpin the scattering assumptions described in Section 3.

### 3 The ice crystal scattering model and forward radar reflectivity model

280 The scattering properties assumed in this study are based on the randomly oriented rosette-aggregate model described in detail by Kleanthous et al. (2024). The model represents an ensemble of rosette aggregates generated using the aggregation model of Westbrook et al. (2004) and constrained to follow the Cotton et al. (2013) mass–dimension relationship, given by  $\text{mass}=0.0257D_m^2$ , where  $D_m$  is the maximum dimension of the ice crystal expressed in SI units, consistent with the Met Office two-moment microphysics scheme, see for details Field et al. (2023). The aggregates are constructed from solid three-branched rosette monomers and are assumed to be randomly oriented in 3-D space.

285 The ensemble comprises of 65 rosette-aggregate realisations spanning maximum dimensions between 10  $\mu\text{m}$  and approximately 1 cm, representative of the dominant habits observed during CCREST-M, as previously discussed in subsection 2.1.2, and consistent with the findings reported by Lawson et al. (2019) and Wagner et al. (2025) in the case of in-situ generated cirrus, typical of the mid-latitudes. Full details of the model generation, morphology, and mass- and area-

dimension power laws are described by Kleanthous et al. (2024). Although referred to as the rosette-aggregate model, this representation does not correspond to a single ice type. As detailed in Kleanthous et al. (2024), the aggregates are composed of rosettes but evolve into different structural forms as they grow, with morphology varying systematically when mass scales with the square of their maximum dimension. For each of the rosette-aggregates, the backscattering cross section,  $\sigma_b(D_m)$ , is computed using the electromagnetic boundary element method (BEM) described by Kleanthous et al. (2022). The rosette-aggregate scattering model has been shown by Baran et al. (2024) to reproduce triple-frequency radar reflectivity measurements at 9, 35 and 94 GHz to within a few dBZ for various mid-latitude and mixed-phase cloud systems that were observed off the north-east coast of the United States during the IMPACTS campaign. Therefore, the rosette-aggregate model is utilised in this paper as the representative ice crystal habit for the retrievals.

### 3.1 The forward radar reflectivity model

From the BEM calculations, solutions found for  $\sigma_b$  are used to forward model the equivalent radar reflectivity factor,  $Z_e$ , where the units of  $Z_e$  are  $\text{mm}^6 \text{m}^{-3}$  and are transformed into units of dBZ via  $10\log_{10}(Z_e)$ , and  $Z_e$  (Atlas et al., 1995; Hong et al., 2008; Baran et al., 2011, and references therein) is calculated following Eq. (1):

$$Z_e = 10^{18} C \int_{D_{min}}^{D_{max}} \sigma_b(D_m) n(D_m) dD_m \quad (1)$$

The measured reflectivities from CAMRa, Kepler, mini-BASTA and GRaCE are provided as equivalent radar reflectivity factor  $Z_e$  in dBZ. These values are computed using the standard definition of water-equivalent reflectivity, i.e., assuming scattering from water spheres and using the same definition as Eq. (1). For our forward model, we adopt the same convention, with  $C = \frac{\lambda^4}{|K|^2 \pi^5}$ , where  $\lambda$  is the incident wavelength in m, and  $|K|^2$  is the dielectric factor of liquid water. This dielectric factor is both frequency and temperature dependent as discussed by Hogan et al. (2006) and in that paper  $|K|^2$  at  $\approx 270$  K for 35 and 94 GHz is 0.88 and 0.67, respectively. At 3 GHz, we use the value of 0.93, and at 200 GHz we use the value used by McCusker et al. (2025) to be consistent with that paper, which was also 0.93. For the cases described by Baran et al. (2024), it was shown that the equivalent radar reflectivity factor has only a weak dependence on temperature and differences in radar reflectivity between the different temperatures was found to be  $\ll 1$  dBZ. The other terms used in Eq. (1) are the backscattering cross section,  $\sigma_b(D_m)$ , in units of  $\text{m}^2$  and  $n(D_m)$ , the assumed PSD in units of  $\text{m}^4$ . The complex refractive indices of ice for 3, 35, 94 and 200 GHz, assuming a temperature of 270 K, have been determined from the tabulation due to Mätzler (2006). This set of refractive indices for ice has been previously recommended by Eriksson et al. (2018). In Eq. (1), the factor  $10^{18}$  is required to convert the units of the integrand into the units of  $Z_e$ . We next consider the PSD assumptions for  $n(D_m)$ , the ML approach and retrieval methodology.

#### 4 The PSD assumptions, machine learning approach, and retrieval methodology

In radar studies, the PSD models used to represent snow crystals or ice aggregates are most commonly gamma or exponential size distributions, see for instance the studies by Heymsfield et al. (2023), and Kozu and Nakamura (1991). The well-known  
 320 gamma size distributions are calculated following Eq. (2):

$$n(D_m) = N_0 D_m^\mu e^{-\lambda D_m} \quad (2)$$

where  $N_0$ ,  $\lambda$  and  $\mu$  represent the intercept parameter, the slope, and the shape parameter of the size distribution, respectively. The units of  $N_0$  and  $\lambda$  are  $m^{-4}$  and  $m^{-1}$ , respectively. In Eq. (2), the exponential PSD is represented when  $\mu=0$ . The PSD parameters  $N_0$ ,  $\lambda$  and  $\mu$  can be estimated from the moments of the PSD, where the  $n^{\text{th}}$  moment of the PSD,  $M_n$ , is calculated  
 325 following Eq. (3):

$$M_n = \int_{D_{min}}^{D_{max}} N(D_m) D_m^n dD \quad (3)$$

It follows from Kozu and Nakamura (1991) that  $\mu$ ,  $\lambda$ , and  $N_0$  can be estimated from the PSD moments following Eqs. (4–6):

$$\mu = \frac{11F - 8 + \sqrt{F(F+8)}}{2(1-F)} \quad (4)$$

where  $F = \frac{M_4^3}{M_3^2 M_6}$ , and

$$330 \quad \lambda = \frac{(\mu+4)M_3}{M_4}, \quad (5)$$

and  $N_0$  is given by:

$$N_0 = \frac{(\lambda^{\mu+4})M_3}{\Gamma(\mu+4)}. \quad (6)$$

where  $\Gamma$  is the gamma function.

Another useful microphysical parameter to derive is the mean mass-weighted diameter ( $D_{mmw}$ ) given by the ratio of  $M_3/M_2$   
 335 on the assumption that mass is proportional to the maximum dimension of the ice crystal raised to the power of two. Here, we consider ice aggregation at radar frequencies assuming the Cotton et al. (2013) mass–dimension power law and this relationship is consistent with our definition of  $D_{mmw}$ . From the PICASSO campaign that took place over the Chilbolton Observatory, from those measured PSDs, all three of the model PSD parameters can be estimated from Eqs. (4–6), and from these the PSDs can be generated from Eq. (2). Therefore, here, we require to retrieve  $N_0$ ,  $\lambda$  and  $\mu$  from the multi-frequency radar reflectivities  
 340 measured during CCREST-M. Note also, that  $F$  from above is determined from  $M_3$ ,  $M_4$  and  $M_6$ , where  $M_4$  for the assumption of ice aggregation is more related to the radar reflectivity since in this case the radar backscatter is proportional to the square of the mass and  $M_6$  further enhances the contribution of larger particles that dominate the radar signal. This is the reason as to why we adopt the definitions of Kozu and Nakamura (1991) in this paper to retrieve the PSDs.

Here, we make use of the in-situ measured PSDs from the PICASSO campaign, which was also conducted over the Chilbolton  
 345 Observatory, where data were collected from ten flights that we utilise in this paper. The approach adopted here is based on the meteorological principle that mid-latitude cirrus clouds observed over the same geographical location should exhibit similar microphysical characteristics when sampled across similar time periods, assuming no significant climate shifts. By

constructing a moment climatology from the PICASSO dataset, we can establish a baseline of cloud properties specific to the Chilbolton region. This climatology should reasonably represent the cloud structures encountered during the CCREST-M period of flying, as both campaigns targeted similar cloud systems in the same geographical location under comparable synoptic conditions during a similar period. Therefore, the moment climatology derived from PICASSO should provide valid prior information for CCREST-M retrievals within the sampled temperature range of the PICASSO campaign.

To construct the moment climatology, we utilise nine PICASSO flights, which are C076, C082, C098, C155, C169, C170, C171, C172, and C174, available from the CEDA website. We use these flights to obtain the profile of moments  $M_2$ ,  $M_3$ ,  $M_4$ , and  $M_6$ , — that is, the variation of these quantities as a function of altitude — as well as profiles of in-cloud temperature,  $T_c$ , pressure,  $p$ , and bulk IWC from the Nevzorov probe. Data from flight C081 is kept as the “unseen” data to evaluate our ML models, as this flight is broadly representative of the others in terms of temperature and IWC ranges. The ML regression-based approach adopted in this study is described in the following sub-section.

#### 4.1 The ensemble of machine learning models and results

The ensemble of ML models we utilise are from Python’s scikit-learn (Pedregosa et al., 2011), this ensemble approach is used to predict the moments of the PSD that will serve as first-guess inputs for the physical retrieval of IWC and the previously described PSD parameters. In this ML model, the feature vector,  $\mathbf{x}$ , consists of:

- (i)  $\log_{10}(D_{mmw})$ , where  $D_{mmw}$  is in units of  $\mu\text{m}$ ,
- (ii)  $\log_{10}(\text{IWC})$ , where IWC is in units of  $\text{g m}^{-3}$ ,
- (iii)  $\log_{10}(p)$ , where  $p$  is in units of hPa, and to be consistent with all other feature spaces,
- (iv)  $\log_{10}(T_c)$ , where  $T_c$  is in units of Kelvin.

For each moment  $\log_{10}(M_n)$  where  $n \in \{2, 3, 4, 6\}$ , we train a separate ML model,  $f_n$ , such that:

$$M_n = f_n(\mathbf{x}) = f_n(D_{mmw}, \text{IWC}, p, T_c) \quad (7)$$

where in Eq. (7) the  $\log_{10}$  symbol has been dropped for reasons of clarity.

For training the ML models we use the PICASSO climatology described above using the nine flights. From these flights we diagnose vertical profiles of the PSD moments  $M_2$ ,  $M_3$ ,  $M_4$ ,  $M_6$ ,  $T_c$ ,  $p$ , bulk IWC from the Nevzorov probe, and  $D_{mmw}$  as defined above. However, in the CCREST-M application,  $D_{mmw}$  is not directly observed and is instead estimated from the empirical  $D_{mmw}(T_c)$  relationship derived from the PICASSO dataset (see sub-section 4.2), so that the same set of predictors can be used. From the feature space given by Eq. (7), the targets of the ML models are the logarithms of the PSD moments,  $\log_{10}(M_n)$  for  $n=2, 3, 4$ , and 6. Although  $D_{mmw}$  is strongly correlated with  $T_c$  in the PICASSO climatology, it is not a deterministic function of  $T_c$ , since for a given  $T_c$  there can be considerable variation in  $D_{mmw}$ . Including both  $D_{mmw}$  and  $T_c$  in vector  $\mathbf{x}$  provides the ML models with complementary information representing the thermodynamics through  $T_c$  and  $p$  and the cloud physics through IWC and  $D_{mmw}$ . For each target moment  $\log_{10}(M_n)$ , we train a separate regression model  $f_n(\mathbf{x})$  using an ensemble of ML models using the default hyperparameter settings to maintain simplicity and reproducibility. The ML models in the ensemble are the random forest regressor, gradient boosting regressor, and support vector regression. For the random forest regressor the

‘shuffle’ parameter is set to ‘false’ as the dataset is a time series and by setting this parameter to ‘false’ we ensure that data from the prediction dataset were not randomly selected to be a part of the training dataset. Therefore, in the presentation of results that follow, the prediction dataset is unseen in the training dataset. The resulting predictions from each of the ML models are simply arithmetically averaged to find the prediction of the ensemble. This approach allows us to predict  $\log_{10}(M_n)$  given  $f(\mathbf{x})$ , required for the retrieval algorithm.

We first evaluate the ensemble approach using a standard 80:20 split of the PICASSO climatology dataset, where 80% of the data are used for the training data, and the remaining 20% are used for the validation dataset. The ensemble predictions for each target moment  $\log_{10}(M_n)$  are compared with the actual values in Fig. 4 (a–d). The hexagonally binned scatter plots show that the ensemble ML predictions cluster tightly about the 1:1 line for all the four moments, which indicates excellent agreement between predicted and true values across the full range of values. The mean-squared errors found for  $\log_{10}(M_2)$ ,  $\log_{10}(M_3)$ ,  $\log_{10}(M_4)$ , and  $\log_{10}(M_6)$  are 0.016, 0.0006, 0.003, and 0.006, respectively, demonstrating that the ensemble of ML models reproduces the logarithmic moments of the PSD with high accuracy. For comparison, using the default random forest model alone resulted in substantially larger mean-squared errors for  $\log_{10}(M_2)$ ,  $\log_{10}(M_3)$ ,  $\log_{10}(M_4)$ , and  $\log_{10}(M_6)$  which were found to be 0.1, 0.103, 0.12, and 0.191, respectively. Clearly, from these results, the ensemble ML model is better to use for the prediction of the required moments than a single ML model. The full results of comparisons are not shown here for reasons of brevity.

Given the results for testing and prediction, the moment predictions for the unseen data from the PICASSO case C081 using the ensemble ML model are presented in Fig. 5 (a–d). Here, rather than presenting statistical representations of how well the predicted moments match the actual moments for C081, we present the moment comparisons in physical space. The figure demonstrates that the predicted re-transformed moments back to physical space compare generally very well with the variability of the actual moments from C081 as a function of temperature. The results depicted in Fig. 5 (a–d) do indeed suggest that ML can be applied to predict the moments of unseen data, and as such ML can provide a good first guess profile for the PSD parameters in a physical retrieval of the microphysics using observed radar reflectivities.

When applying the trained models to the CCREST-M cases, the same feature vector  $\mathbf{x}$  is constructed using profiles of  $T_c$  and  $p$  from the dropsondes, together with profiles of IWC and  $D_{mmw}$  derived from the 3 GHz radar reflectivity and a separate temperature-based polynomial model, respectively. The prediction of  $D_{mmw}$  from  $T_c$  is next described in sub-section 4.2 and the retrieval methodology in physical space is described in the sub-section 4.3. In sub-section 4.4, the retrieval of IWC from the 3 GHz radar is then described. A schematic overview of the full retrieval framework, from PICASSO training to the CCREST-M multi-frequency radar retrieval, is depicted in Fig. 6.

410

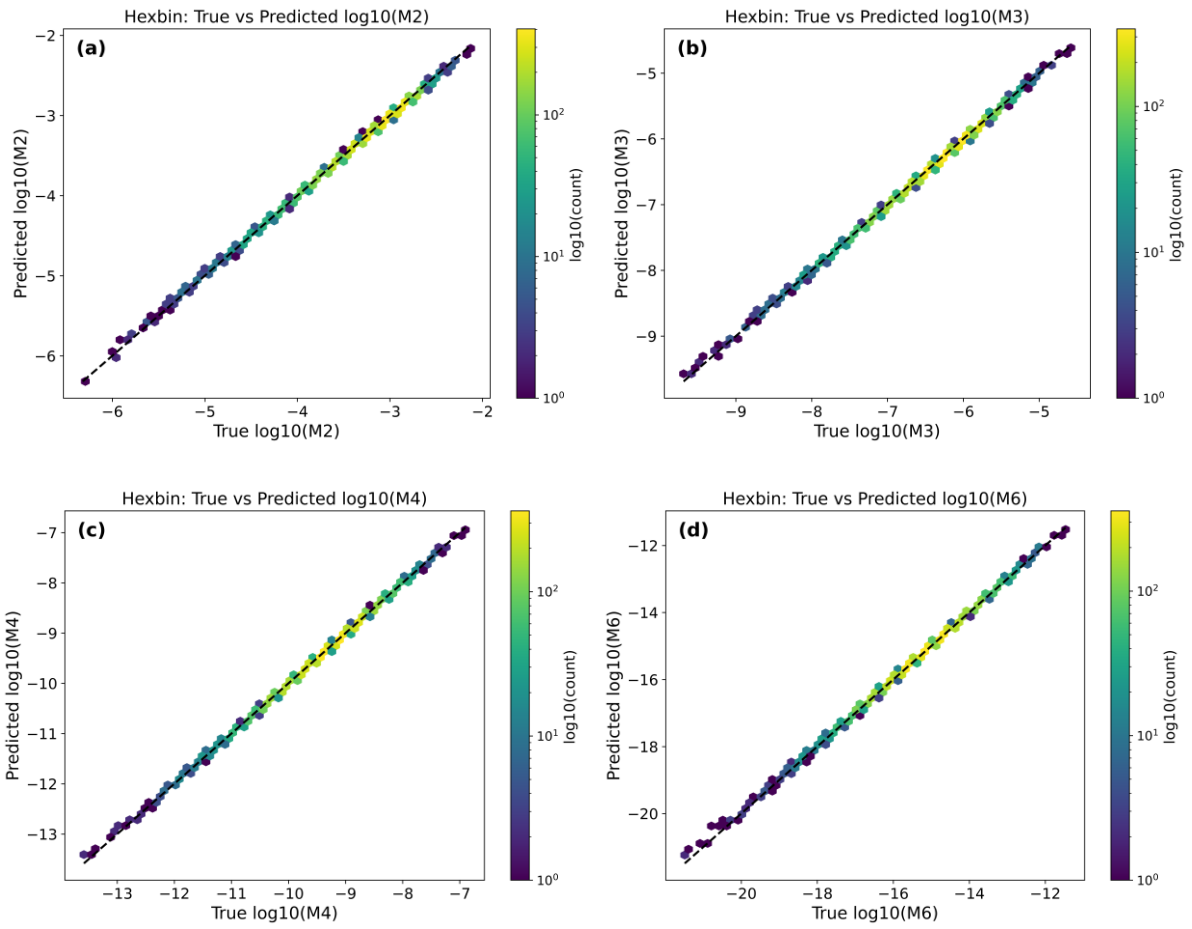


**Figure 4** Hexagonally binned scatter plots of predicted versus true  $\log_{10}(M_n)$  from the ensemble of ML models for the PICASSO validation subset for (a)  $n=2$ , (b)  $n=3$ , (c)  $n=4$ , and (d)  $n=6$ . The colour scale shows the logarithm to the base 10 of the number of points in each of the hexagonal bins and the dashed line in each of the panels indicates the 1:1 line.

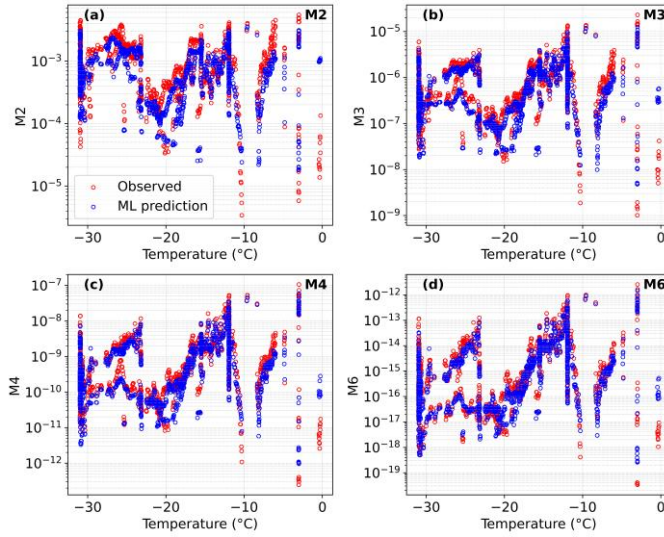


**Figure 5** Comparison of the re-transformed observed (open red circles) moments from C081 and predicted moments (open blue circles) using the ensemble-averaged ML predictions plotted against the in-cloud temperature for (a)  $M_2$ , (b)  $M_3$ , (c)  $M_4$  and (d)  $M_6$ . The key to each of the panels is shown in the bottom-left corner of panel (a).

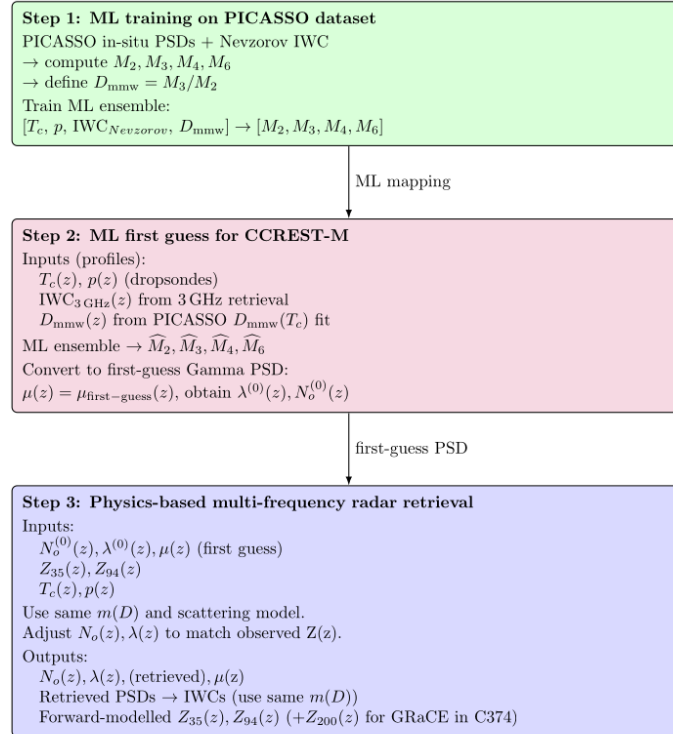


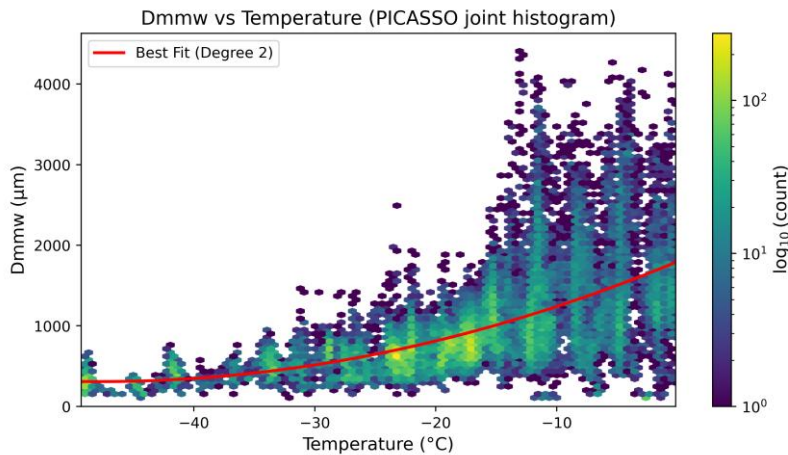
**Figure 6** A schematic overview of the retrieval framework. Step 1: an ensemble ML model is trained on the PICASSO dataset using in-situ PSDs and the Nevzorov IWC to compute the PSD moments  $M_2$ ,  $M_3$ ,  $M_4$  and  $M_6$  and the mean mass-weighted diameter  $D_{mmw}=M_3/M_2$ . Step 2: for each CCREST-M case, profiles of  $T_c$ ,  $p$ , 3 GHz-retrieved IWC and  $D_{mmw}(T_c)$  are passed through the ML ensemble to predict the moments, which are converted into first-guess gamma PSD parameters, with  $\mu(z) = \mu_{\text{first guess}}(z)$ , where  $z$  is the altitude, and corresponding  $\lambda^{(0)}(z)$  and  $N_o^{(0)}(z)$ . Step 3: a physics-based multi-frequency radar retrieval adjusts  $N_o(z)$  and  $\lambda(z)$  using the same  $m(D)$  and scattering model so that simulated reflectivities  $Z_{35}(z)$  and  $Z_{94}(z)$  match the observations, yielding retrieved PSD parameters, PSDs and estimated IWCs, and forward-modelled reflectivities.

## 4.2 Estimating the profile of $D_{mmw}$

To obtain a first-guess profile of  $D_{mmw}$  we exploit the observed relationship between  $D_{mmw}$  and the in-cloud temperature  $T_c$  in the PICASSO dataset, where  $D_{mmw}=M_3/M_2$ . Since we use  $T_c$  to be the only predictor for  $D_{mmw}$ , the underlying relationship is expected to be a smooth function of temperature rather than a highly structured one. Therefore, a low-order polynomial is fitted to the PICASSO  $D_{mmw}(T_c)$  dataset. Polynomials from degree 1 to degree 10 were tested and each fit was evaluated using the coefficient of determination,  $R^2$ , the root mean-square error, RMSE, and a k-fold cross-validation score. It was found that a low-order polynomial provided a good fit, with  $R^2=0.40$ , and  $RMSE=475 \mu\text{m}$ , and positive cross-validation performance, while higher-degree polynomials yield only marginal improvements in RMSE and increasingly unstable cross-validation statistics indicative of overfitting. The resulting quadratic relation between  $D_{mmw}$  (in  $\mu\text{m}$ ) and  $T_c$  (in  $^\circ\text{C}$ ) is

$$D_{mmw}(T_c)=1797.5+62.33T_c+0.652T_c^2.$$

Figure 7 depicts the best-fit curve overlaid on the observed PICASSO distribution of  $D_{mmw}$  as a function of  $T_c$ . It can be seen from the figure that the fit captures the overall increase of  $D_{mmw}$  with temperature, while the substantial scatter about the curve, especially at the warmer temperatures, reflects the differing cloud bulk and microphysical properties encountered during each of the PICASSO flights.



445 **Figure 7** Joint distribution of  $D_{mmw}$  and in-cloud temperature  $T_c$  for the PICASSO dataset. The coloured hexagons show a two-dimensional histogram of  $D_{mmw}$  versus  $T_c$ , shaded by  $\log_{10}(\text{count})$  as indicated by the colour bar on the right-side of the figure. The red line shows the best-fit quadratic polynomial:  $D_{mmw}(T_c)=1797.5+62.33T_c+0.652T_c^2$ .

In the CCREST-M retrievals, this quadratic relation is used to predict a deterministic first-guess profile of  $D_{mmw}$  from the dropsonde temperatures. As with the 3 GHz IWC retrieval, the role of  $D_{mmw}$  is to keep the ML-based PSD moment estimates close to representative values by providing a good starting point, while the subsequent multi-frequency optimisation adjusts the PSD parameters to match the observed reflectivities. We next describe the physically based dual-frequency retrieval of the PSD parameters given the ML first guess PSD parameter profiles.

### 4.3 Retrieval methodology in physical space

455 For the dual-frequency retrieval methodology we utilise the 35(z) and 94(z) GHz mean profile radar data and we employ a gamma size distribution model for the PSD as given by Eq. (2). The forward model  $F$  is given by Eq. (1). Here, the retrieval process begins with an initial guess profile derived from the ensemble of ML moment predictions, which are transformed into the PSD parameters  $\mu(z)$ ,  $\lambda(z)$ , and  $N_o(z)$  via Eqs. (4–6), respectively, to provide the starting values for the retrieval. The algorithm then retrieves optimal values of  $N_o(z)$  and  $\lambda(z)$  by minimising the differences between the forward model predictions and the observed radar reflectivities at both 35 and 94 GHz simultaneously.

The minimisation problem can be formally expressed as:

$$(N_o(z), \lambda(z))^{retrieved} = \arg \min (N_o(z), \lambda(z)) \|F(N_o(z), \lambda(z)) - Z_{obs}(35(z), 94(z) \text{ GHz})\|, \quad (8)$$

where  $Z_{obs}$  represents the observed 35 and 94 GHz radar reflectivities, and the retrieval results are only accepted when the difference between the forward model and observations satisfies the following condition:

$$465 \|F(N_o(z), \lambda(z)) - Z_{obs}(35(z), 94(z) \text{ GHz})\| < 1dBZ \quad (9)$$

To solve this minimisation problem, we implement the Nelder-Mead simplex algorithm, which is a derivative-free optimisation method. The Nelder-Mead approach, see Nelder and Mead (1965), iteratively refines a simplex (a geometric figure in  $n$ -dimensional space with  $n+1$  vertices) to find the minimum of our objective function. Also, the Nelder-Mead algorithm demonstrates robust performance in the presence of noise and other irregularities in the objective function, making this method appropriate for the retrievals where observational uncertainties are inherent. In the next sub-section, we describe the method to retrieve the IWC from the 3 GHz radar using the optimisation presented here.

### 4.4 Retrieval of the IWC profiles

To retrieve the IWC, we utilise the 3 GHz radar reflectivities, and for this retrieval the climatologically averaged PSD parameters found for  $N_o$ ,  $\lambda$ , and  $\mu$ , which have been derived from the PICASSO dataset are used to initialise the retrieval of  $\lambda$ , where  $\mu$  is set to its climatologically averaged value of 2.33 throughout the retrieval. In the case of  $N_o$ , this parameter is allowed

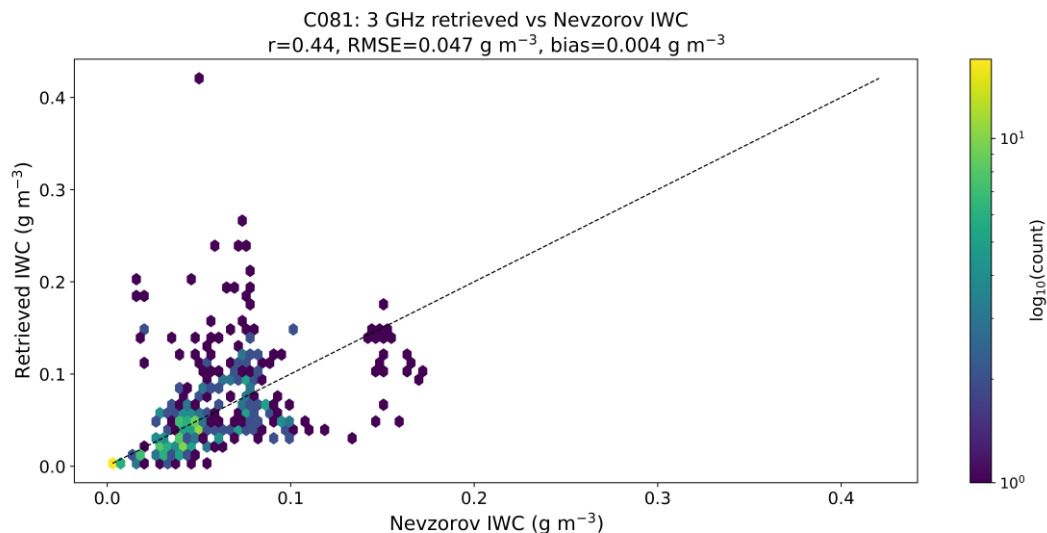
to vary with temperature following Hogan et al. (2006), where we initialise and adjust  $N_o$  according to the relationship  $N_o = 2 \times 10^{14} \exp(-0.122T_c)$ , and the numerical factor in the relationship is derived from the PICASSO climatology using the  $N_o$  equation from Kozu and Nakamura (1991),  $T_c$  is in units of degree Celsius. This retrieval uses the same forward-model retrieval framework as the full multi-frequency retrieval described in sub-section 4.3, but in this case the radar observation consists solely of the 3 GHz radar reflectivities. The retrieval of IWC here is to provide IWC profiles as an input feature to the ensemble of ML models.

The gradient  $\lambda$  is retrieved by minimising the difference between  $\|F(3 \text{ GHz}) - Z_{\text{obs}}(3 \text{ GHz})\|$ , where  $F(3 \text{ GHz})$  and  $Z_{\text{obs}}(3 \text{ GHz})$  are the forward model given by Eq. (1) and observed radar reflectivities at 3 GHz, respectively, with retrievals only being accepted when these differences are less than 1 dBZ. Thus, using the retrieved  $\lambda$ , estimated  $N_o$ , and constant  $\mu$ , we apply the gamma PSD to estimate the IWC using:

$$IWC = \int_{D_{\min}}^{D_{\max}} m(D_m)n(D_m)dD_m \quad (10)$$

where in Eq. (10),  $m(D_m)$  is the mass–dimension relationship from Cotton et al. (2013), i.e.,  $m(D_m)=0.0257D_m^2$ . This mass power law is the same as the mass power law used to construct the rosette aggregate model described in Section 3, and the rosette aggregate model is used to predict the backscattering coefficients at 3 GHz using the well-known Rayleigh scattering, assuming the equivalent ice mass spherical radius.

To test our retrieval of IWC using the 3 GHz radar data we use collocated radar and aircraft observations from the PICASSO flight C081. Figure 8 compares the hexagonally binned retrieved IWC with the in-situ IWC measured by the Nevzorov probe for all samples above 3200 m. We focus on altitudes greater than 3200 m owing to the presence of a melting layer at lower altitudes. We specifically target retrievals outside of the melting layer because during CCREST-M we deliberately avoided this region, as it is too complex to simulate accurately assuming the rosette aggregate model. Moreover, the comparisons in Fig. 8 include only data points where radar observations were recorded within 36 seconds of the aircraft position, within 50 m of the aircraft altitude, and within the same distance from the Chilbolton Observatory site. The hexagonally binned scatter plot shows that most points lie close to the 1:1 line, with a RMSE difference of  $0.047 \text{ g m}^{-3}$  and a negligible bias of just  $0.004 \text{ g m}^{-3}$ , but with a moderate  $r=0.44$ , the latter value is probably owing to the limited range of sampled IWC because of the choice of the minimum altitude. However, in absolute terms the 3 GHz retrieval of IWC reproduces the Nevzorov-derived IWC with small errors over the ice layer of interest. Moreover, in the retrieval framework, the 3 GHz retrieved IWC profile is used only as a constraint on the first-guess PSD moments for the multi-frequency optimisation described in sub-section 4.3, so the IWC profile does not need to be completely correct but rather provide a reasonable estimate of the profile of ice mass within the cloud, which the retrieval achieves as Fig. 8 depicts.



505

**Figure 8** Hexagonally binned scatter plots of retrieved IWC from the 3 GHz radar plotted against in-situ Nevzorov-derived IWC for the PICASSO flight C081 and for altitudes greater than 3200 m. The colour scale on the right-side shows the  $\text{Log}_{10}$  of the number collocated samples per bin, with the dashed line indicating a slope of unity. The correlation coefficient,  $r$ , the root mean square error (RMSE) and the bias are shown at the top of the figure.

510

In the next section, the retrieval methodologies outlined in this section and sub-sections are applied to the three in-situ cases that were sampled during the CCREST-M campaign of flying.

### 5 The PSD parameter retrievals and comparisons with aircraft data

Here, the retrieval methodology outlined in Section 4 is applied to the zenith-pointing 3, 35 and 94 GHz mean radar reflectivity profiles for the three CCREST-M cases (C374, C379, C382). For each of the flights, the zenith-pointing radar profiles are taken from periods when the FAAM BAe-146 aircraft executed figure-of-eight overpasses above cloud top while all three radars operated in zenith pointing mode.

For C374, these figure-of-eight overpasses occurred in three blocks between about 10:24–10:43 UTC, 11:29–11:33 UTC, and 11:37–11:42 UTC at altitudes near to 10 km. After the third set of overpasses, the aircraft flew a single profile descent through the cloud as described in Section 2. For C379, the aircraft flew two blocks of figure-of-eight overpasses between approximately 16:10–16:26 UTC and 17:07–17:28 UTC. These were followed by in-situ sampling along the 270° radial, which began at about 17:33 UTC and lasted until about 18:11 UTC, and consisted of stepped descents with straight-and-level runs of several minutes at successive levels. Finally, for C382, the aircraft first completed the figure-of-eight overpasses between

520

about 15:00 and 15:26 UTC and again between 16:17 and 16:28 UTC while the radars were in Zenith mode. The subsequent  
525 in-situ sampling along the 246° radial began at 16:33 until about 17:09 UTC, following a similar pattern to C379.

As alluded to previously, only a single aircraft was available, and from the flight patterns and timings described above, the  
in-situ PSDs and the zenith-retrieved PSDs are not strictly collocated in time and space, instead they represent different  
realisations of the same frontal ice cloud systems. The in-situ legs typically lag the initial zenith-dwell period by about 60  
minutes but closely follow the final zenith-dwell period by about 5 minutes. Horizontally, each in-situ straight and level run  
530 lasts about 9 minutes at an airspeed of about 100 ms<sup>-1</sup>, corresponding to along-track distances of order 50 – 60 km along the  
selected Chilbolton radial before the aircraft turns to begin the next leg. Thus, the in-situ sampling spans a substantial segment  
of the radar radial rather than a single point above the Chilbolton site. For each flight we therefore compare the retrieved PSDs  
statistically with the in-situ composited PSDs, rather than on a point-by-point basis, and retrievals that are below the IWC  
threshold of 0.002 g m<sup>-3</sup> are rejected for the reasons given in sub-section 2.1. The following sub-sections present the ensemble  
535 ML moment predictions, retrieved PSDs, and their comparisons with the in-situ moments and PSDs for each case.

## 5.1 The case C374

For C374, we begin by comparing the ensemble ML predictions of the target moments with those derived in-situ from the  
composite PSDs. Following this, the retrieved PSDs are evaluated against the in-situ composite PSDs as a function of  
temperature, the dual-frequency residuals are also examined along with comparisons of IWCs estimated from the retrieved  
540 PSDs with the Nevzorov-derived IWCs.

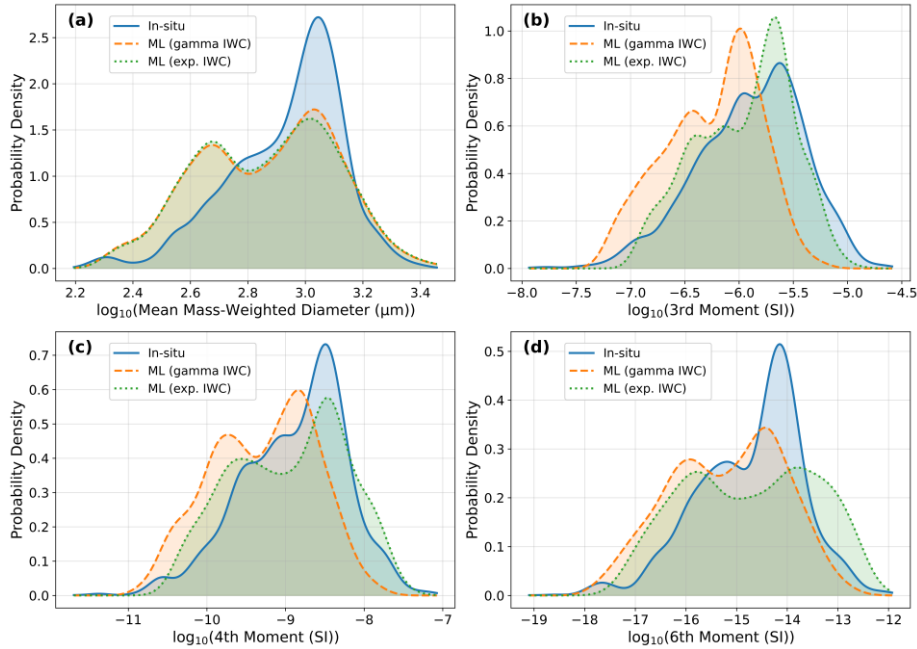
### 5.1.1 Moment estimations and comparisons with aircraft data

The ensemble ML model predictions of  $D_{mmw}$ ,  $M_3$ ,  $M_4$ , and  $M_6$  are compared with the derived in-situ estimated moments from  
the composite PSDs in Fig. 9 (a–d), the comparisons are shown as normalised probability density functions (PDFs), where the  
area under the curve equates to unity. Here the in-situ distributions are formed from all PSDs measured during the stepped-  
545 descent legs, while the ML distributions are formed from the ML predictions from the zenith-radar retrieval levels over about  
the same altitude range. To assess the sensitivity of the ML predictions to the assumed shape of the PSD in the 3 GHz IWC  
retrieval, results are shown for both gamma and exponential PSD assumptions. We consider altitudes greater than 1 km, and  
in-cloud temperatures warmer than -50°C.

Under the gamma PSD assumption, the ML ensemble predictions compare favourably with the in-situ moments, with similar  
550 distribution spreads, indicating that the ML captures to some extent the natural variability observed in the in-situ data. The  
central tendency is well captured for  $D_{mmw}$  and  $M_6$  as shown in panels (a) and (d) but is slightly underestimated for  $M_3$  and  $M_4$   
in panels (b) and (c). A systematic bias is nonetheless evident across all the parameters, for instance, for  $D_{mmw}$  the in-situ mean  
is 941  $\mu\text{m}$  compared with 734  $\mu\text{m}$  for the ensemble ML model, and similar leftward shifts are apparent in panels (b), (c), and  
(d).

555 For the case of the exponential PSD assumption, we see that this PSD assumption mitigates the previous negative biases for the higher-order moments. The central tendencies of the ML predictions for  $M_3$ ,  $M_4$ , and  $M_6$  shift towards the in-situ values, and the distribution spreads improve correspondingly. For  $D_{mmw}$ , which is a ratio of moments, the change in PSD assumption has little impact as shown in panel (a). The improvement at the high-order moments is likely owing to the exponential distribution predicting a greater occurrence of larger particles than the gamma distribution.

560



565 **Figure 9** The normalised PDFs of the logarithm (base 10) of the predicted and observed moments for case C374. In-situ size distributions derived from the composite PSDs are shown as solid blue lines and a blue shaded fill. The ML ensemble predictions are presented for the gamma and exponential PSD assumptions used in the retrieval of the 3 GHz IWC. The gamma and exponential PSD assumptions are shown as the orange-dashed line with orange fill, and green-dashed line with green fill, respectively. Comparisons are presented for (a)  $D_{mmw}$ , (b)  $M_3$ , (c)  $M_4$  and (d)  $M_6$ . The key is shown in the top-left corner of each panel.

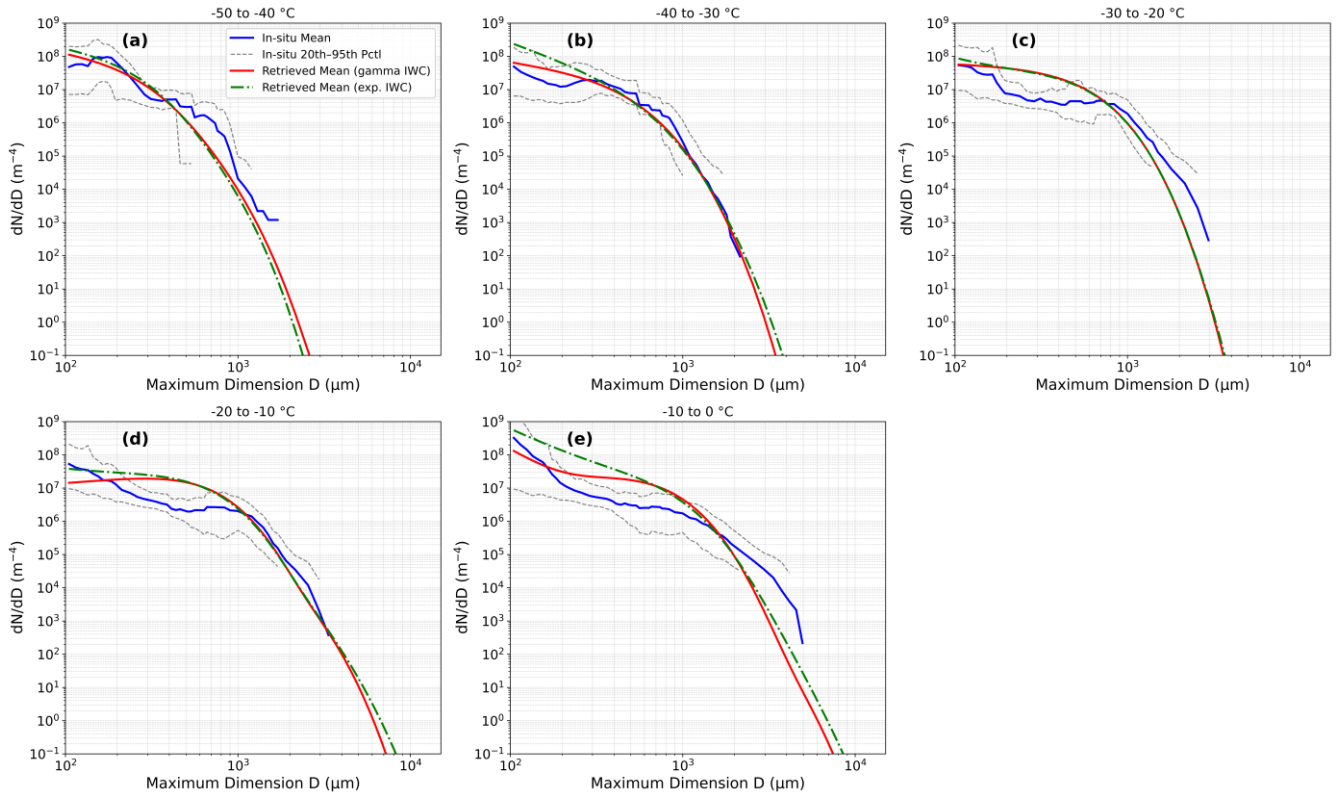
570 The impact of changing the shape assumption of the PSD on the retrieval of IWC and how this manifests itself on the retrieved PSDs as a function of temperature will be examined in the next sub-section.

### 5.1.2 Retrieval of the PSDs and comparisons with the in-situ composite PSDs

Now that we have derived the first-guess profiles for the PSD parameters from the profiles of IWC,  $D_{\text{mmw}}$ ,  $T_c$ , and  $p$ , the PSD parameters,  $N_0$ ,  $\lambda$  and  $\mu$  are input to the dual-frequency retrieval as described in sub-section 4.3, only varying  $N_0$  and  $\lambda$  while  
575 keeping the profile of  $\mu$  as the first guess. Figure 10 (a – e) presents a comparison between retrieved and in-situ composite PSDs for the flight C374, as a function of temperature for maximum dimensions greater than 100  $\mu\text{m}$ . The retrieved PSDs assume gamma and exponential size distributions for the retrieval of the IWC profiles using the 3 GHz radar and only include retrievals greater than 1 km in altitude to focus on the primary iced regions of this frontal cloud system and IWCs greater than 0.002  $\text{g m}^{-3}$ . To provide robust statistical comparisons, the analysis presents the mean and the in-situ interpercentile range (20<sup>th</sup>  
580 to 95<sup>th</sup> percentiles) for both sets of data across five temperature bins: -50 to -40°C, -40 to -30°C, -30 to -20°C, -20 to -10°C, and -10 to 0°C. This choice of in-situ interpercentile range retains the bulk of the distribution while excluding the retrievals in the lowest tail, and a small number of very large values which may arise from occasional misfits. Thus, the 20<sup>th</sup> to 95<sup>th</sup> percentile range provides a clearer view of the central behaviour of the retrievals relative to the in-situ composites without being overly influenced by a small number of extremes. Also, the temperature stratification allows examination of retrieval performance as  
585 a function of temperature, and it is the temperature that chiefly determines the microphysics. Here, we focus on the PSDs themselves rather than plotting the corresponding moments of the retrieved PSDs after the 35 and 94 GHz fitting. This is because the moments are effectively summarised by the PSD comparisons shown in Fig. 10 (a-e) and so a moment-by-moment comparison would therefore be redundant.

For the case of assuming the gamma size distribution for the retrieval of IWC at 3 GHz the comparisons presented in Fig. 10  
590 (a – e) show generally good agreement between the retrieved and in-situ PSDs across most of the temperature bins. For instance, the mean retrieved PSD is largely within the interpercentile range of the in-situ PSDs for most of the considered temperatures. The most notable systematic overestimations of the retrieved number concentrations relative to the in-situ concentrations occur for the sizes of several hundred  $\mu\text{m}$  at the warmer temperatures, especially as seen in Fig. 10 (c – e). In general, the figure shows that across all temperature regimes there is considerable overlap in the variability captured by the  
595 retrieved and in-situ PSDs, suggesting that the retrieval method successfully represents the natural variability in PSD characteristics, even when absolute concentrations might be biased at some of the sizes.

In the case of the exponential PSD being assumed to retrieve the IWC at 3 GHz, the exponential size distribution assumption produces notable changes in representing smaller ice crystal number concentrations at the warmer temperature bins. Specifically, it tends to overestimate number concentrations for sizes less than about 1000  $\mu\text{m}$  and above several thousand  
600 microns, as shown in panels (b, d, e).



605 **Figure 10** Comparison of retrieved and in-situ composite PSDs for flight C374 as a function of temperature. Retrieved mean  
 PSDs assuming the gamma and exponential PSDs for the retrieval of the 3 GHz IWC are shown as red solid lines and green-  
 dotted lines, respectively. The composite mean in-situ PSDs are shown as solid blue lines and the in-situ 20<sup>th</sup> and 95<sup>th</sup>  
 percentiles are shown as the grey dashed lines. Results are presented for the temperature bins (a) -50 to -40°C, (b) -40 to -30°C,  
 (c) -30 to -20°C, (d) -20 to -10°C, and (e) -10 to 0°C. The key is shown in the upper-right of panel (a).

610

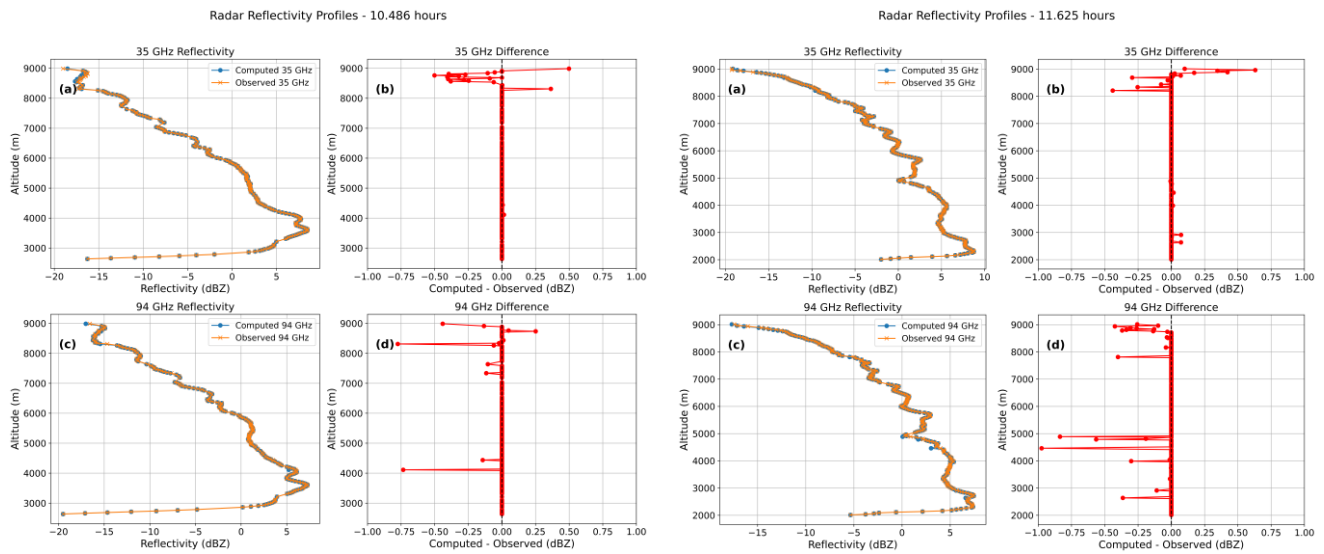
To further evaluate the retrieved PSDs assuming the gamma or exponential PSD for the retrieval of IWC at 3 GHz, we  
 compare the mean and standard deviation,  $\sigma$ , of the IWC computed from the retrieved PSDs, using Eq. (10) assuming the  
 Cotton et al. (2013) mass–dimension power law, within each temperature bin, with corresponding in-situ IWC statistics  
 measured by the Nevzorov probe. The results of these comparisons are presented in Table 2, along with the numbers of  
 615 retrieved PSDs and in-situ measurements within the interpercentile range used in the calculation for each of the temperature  
 bins.

620 **Table 2** Comparison of retrieved ( $R_{\gamma/exp}$ ) and in-situ (In) statistics for the mean and standard deviation of the IWC in each temperature bin, with the total number (num) of retrievals ( $num_{\gamma/exp}$ ) and measurements filtered into each temperature bin.

Temp Bin (°C)	In-situ num	R num <sub>gamma</sub>	R num <sub>exp</sub>	$R_{\gamma} \overline{IWC} \pm \sigma$ (g m <sup>-3</sup> )	$R_{exp} \overline{IWC} \pm \sigma$ (g m <sup>-3</sup> )	$In \overline{IWC} \pm \sigma$ (g m <sup>-3</sup> )
-50 to -40	124	56	49	0.011±0.005	0.015±0.006	0.016±0.004
-40 to -30	315	99	96	0.021±0.011	0.025±0.015	0.03±0.007
-30 to -20	238	114	110	0.070±0.02	0.064±0.02	0.049±0.015
-20 to -10	661	129	143	0.098±0.027	0.096±0.027	0.059±0.019
-10 to 0	540	163	157	0.148±0.034	0.181±0.046	0.084±0.037

Under both the gamma and exponential PSD assumptions, Table 2 demonstrates that for the integral property IWC, the retrieved PSDs generally compare well with the in-situ Nevzorov measurements in the two coldest temperature ranges. At the warmer temperatures, both assumptions tend to overestimate the in-situ mean IWC values by varying amounts, although the differences remain within a factor of two. However, despite this, there is substantial statistical overlap between the retrieved and in-situ IWC ranges for both PSD assumptions. The only exception being the exponential PSD assumption at the warmest temperature bin. Figure 10 and Table 2 illustrate the trade-off at different temperature bins in selecting an optimal size distribution that performs well across the full range of ice cloud conditions.

630 To evaluate the consistency of the retrieval framework, it is instructive to examine how well the forward-modelled radar reflectivities at 35 and 94 GHz compare with observations when using the retrieved PSDs and scattering model. Figure 11 (left–right panels) depicts the radar reflectivity profiles and their residuals, assuming the gamma PSD for the 3 GHz retrieval of IWC, computed from Eqs. (1) and (9), for accepted retrievals as a function of altitude for two of the six coincident overpasses between the aircraft and zenith-pointing radars. In Fig. 11 (left–right panels), we show residuals for the first (10.49 hrs) and last (11.63 hrs) overpass times, as these are representative of all six overpass times.



635

**Figure 11** Comparison of forward model simulations (blue lines and circles) and observations (orange lines and circles) with their corresponding residuals (red lines and circles) as a function of altitude for the 35 (a, b) and 94 GHz (c, d) radars. Times correspond to coincident aircraft overpasses for 10.49 hrs (left panels) and 11.63 hrs (right panels). The key is shown in the top-right of each panel.

640

The radar reflectivity comparisons demonstrate generally good agreement between the forward-modelled and observed reflectivities across most altitude levels. At both of the frequencies, the simulated reflectivities closely follow the observed profiles through the main parts of the ice cloud, with residuals typically well within  $\pm 0.5$  dBZ. This agreement shows that the retrieved PSDs and scattering model are appropriate for the bulk of the ice cloud. However, at the cloud top regions and on some occasions in the cloud bottom regions, in particular panel (d) at the time of 11.625 hrs, below about 5 km, residuals show increased variability and magnitude, with some approaching -1 dBZ in those regions. At the cloud top regions, the radars become less sensitive, owing to the smaller sizes and concentrations of ice crystals making retrievals in those regions more problematic. The consistency of this pattern across all of the six times suggests that the greater deviations of the residuals from near-zero are systematic rather than random, indicating the fundamental limitation of the dual-frequency retrievals in regions where the ice crystals are small and radar sensitivity is reduced. At cloud bottom, ice crystal type may also be changing causing the retrievals to become more problematic where this could be occurring. The computed and measurement residuals are not shown for the exponential PSD assumption as these are very similar to those already presented in Fig. 11.

650

One radar frequency operated during C374 but not used in any retrievals was the G-band GRaCE radar, providing an excellent independent validation of the retrieved PSDs and scattering model. The radar operation during C374 and applied attenuation corrections have been fully discussed by McCusker et al. (2025), and so will not be repeated here. However, in this paper, the G-band reflectivities have been corrected for ice attenuation using the rosette aggregate model. The forward-modelled GRaCE

655

radar reflectivity using the retrieved filtered PSDs and the randomly oriented rosette aggregate model is compared with the GRaCE observations in Fig 12. The figure compares the forward-modelled 200 GHz radar reflectivity, computed from the retrieved PSDs assuming both the gamma and exponential PSD assumptions, with the GRaCE radar observations. The comparisons show time-averaged mean profiles, the standard radar reflectivity measurement uncertainty of  $\pm 1$  dBZ, and the interpercentile ranges for both the observations and simulations. The simulations were averaged using the thresholds of 0.1 decimal hours for time and 100 m for the altitude to provide meaningful statistical comparisons. The comparisons were further restricted to times before approximately 11:45 UTC, beyond which the cloud evolved down to 2 km, a complex configuration which resulted in precipitation at later times. Above approximately 4.5 km the calculated reflectivities sit within or very close to the measured  $10^{\text{th}} - 90^{\text{th}}$  percentile envelope, and the gamma and exponential assumptions produce very similar forward-modelled profiles. For the upper part of the cloud, this level of agreement provides strong support for the rosette-aggregate scattering model and retrieved PSDs. Indeed, Fig. 3 (a) (upper panels), show the predominant habits to be rosettes and small rosette aggregates, providing further evidence for the choice of scattering model. Below approximately 4.5 km, the calculated mean reflectivities trend higher than the measured mean, although the calculated  $10^{\text{th}} - 90^{\text{th}}$  percentile envelopes continue to overlap the measured envelope just above 3 km. These discrepancies as shown by Fig. 3 (a) in the lower parts of the clouds, are likely owing to the presence of more irregular dendritic particles and snowflakes, which are not represented by the rosette-aggregate model used here. Also, the two PSD assumptions in the lower part of the cloud follow each other closely, indicating that this independent validation cannot discriminate between the two PSD shape assumptions.

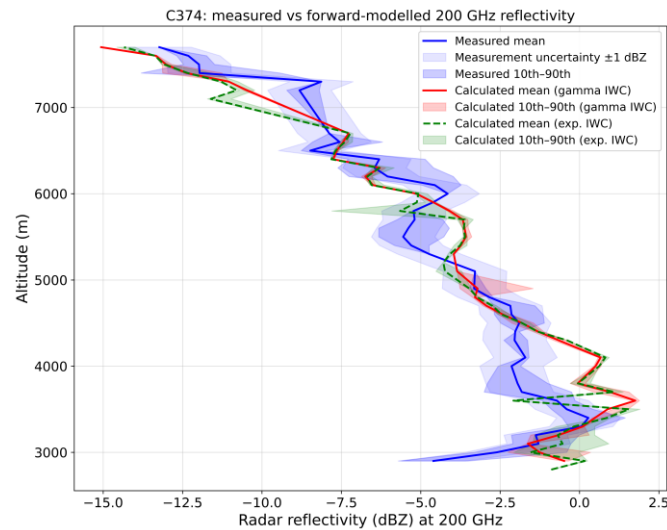


**Figure 12** Comparison of the time-averaged forward model simulations (red, green lines, and shade) assuming the retrieved PSDs, assuming the gamma (red lines) and exponential (green lines) PSDs for the retrieval of IWC at 3 GHz with the 200 GHz GRaCE radar observations (blue lines and shade). The key is shown in the bottom-left of the figure.

## 5.2 The case C379

For C379, the 94 GHz radar experienced severe attenuation owing to precipitation and collection of water on the radar dome that occurred at about 0900 UTC. More prolonged precipitation occurred from about 1700 UTC for the rest of the day of between about several to 1 mm/hr, as measured by the drop counting rain gauge at Chilbolton (McCusker et al. 2025). There was no rain after 1000 UTC until about 1600 UTC, when more episodic precipitation was measured by the rain gauge. The occurrence of lower-level liquid water cloud can clearly be seen in Fig. 2 (middle panel). Since this precipitation after 1600 UTC occurred during the figure-of-eight overpasses and the aircraft in-situ sampling period, dual-frequency retrievals were not possible. Consequently, only single-frequency retrievals using the 35 GHz radar are employed for this case. We begin with ML to predict the PSD parameters and use these to generate the PSDs that are compared with the in-situ composite PSDs, following the same analysis as used in sub-section 5.1.

### 5.2.1 Moment estimations and comparisons with aircraft data for C379

Following the methodology for the case C374, we examine the ML performance in predicting the PSD moments for single-frequency retrievals. Consistent with C374, IWC was optimally retrieved using an exponential size distribution with the 3 GHz radar as input to the ML.

Figure 13 (a–d) depicts the normalised PDFs, comparing the ML-predicted moments with those derived from the in-situ PSDs for  $D_{mmw}$ ,  $M_3$ ,  $M_4$ , and  $M_6$ . The ML-predicted  $D_{mmw}$  distribution exhibits a bimodal structure with the primary peak positioned close to the in-situ peak. For the higher-order moments  $M_3$ ,  $M_4$ , and  $M_6$ , the ML-predicted distribution spreads align very well with the in-situ derived moments, suggesting the relative variability patterns are very well captured by ML for this case.

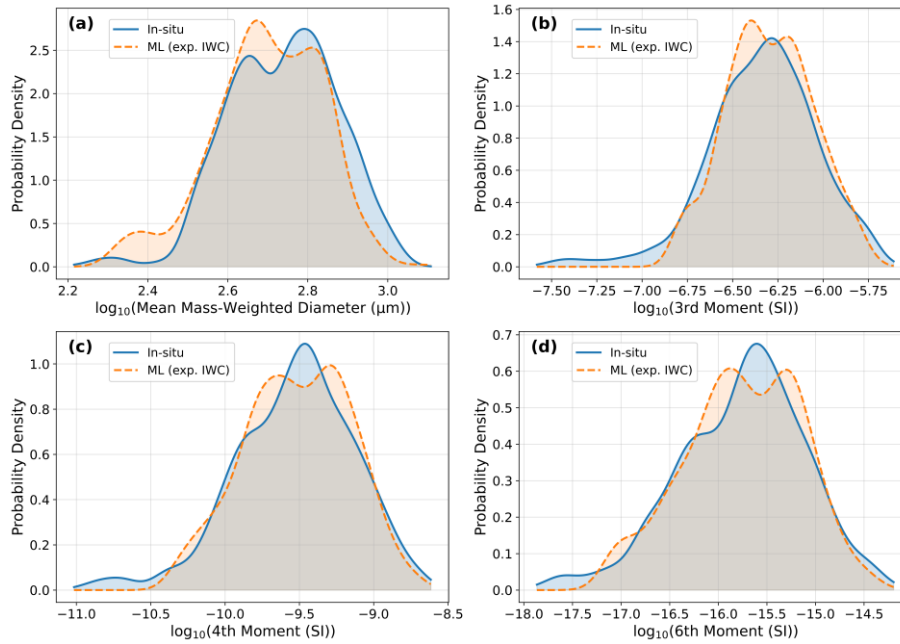


**Figure 13** Same as Fig. 9, but for the case C379 and using the exponential size distribution to retrieve IWC at 3 GHz.

### 700 5.2.2 Single-frequency retrievals of the PSDs and comparisons with the in-situ composite PSDs for C379

For case C379, we use the 35 GHz radar to retrieve one PSD parameter. The IWC profile first-guess is retrieved from the 3 GHz radar assuming the gamma size distribution. The ML provides first-guess profiles for  $N_0$  and  $\mu$ , while the slope parameter  $\lambda$  is optimised using Eq. (8) to minimise differences between the forward model simulations and the 35 GHz radar observations.

705 Figure 14 (a–d) compares the single-frequency PSD retrievals with the in-situ measurements for four temperature bins (-50 to -40°C, -40 to -30°C, -30 to -20°C and -20 to -10°C).

710

715

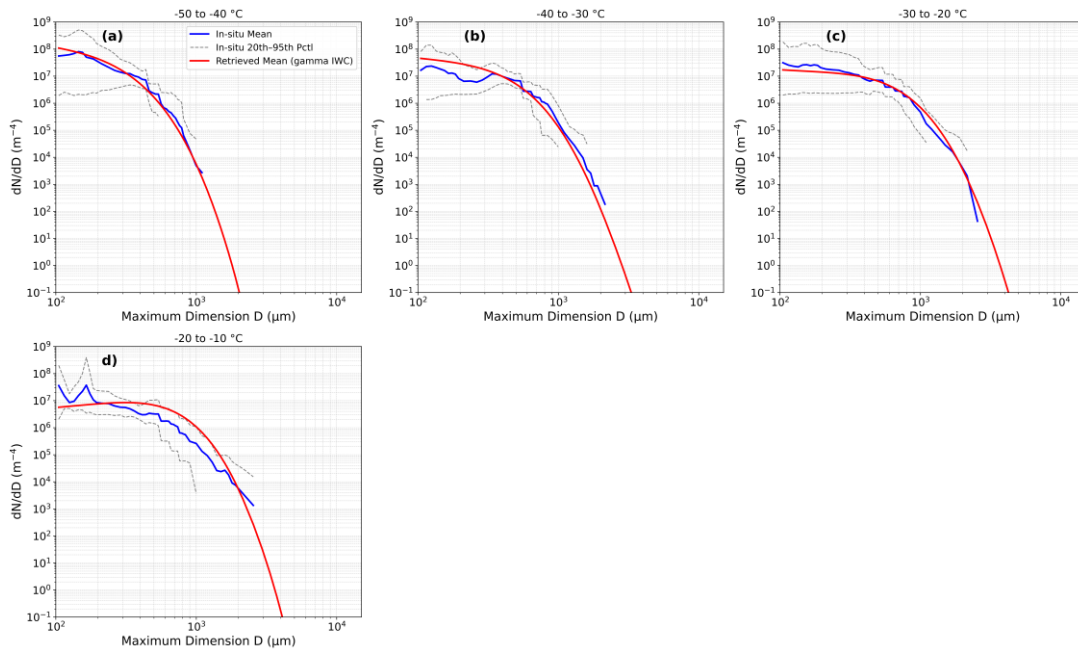


**Figure 14** Same as Fig. 10, but for the single-frequency retrieval using the 35 GHz radar and assuming the gamma size distribution for the retrieval of IWC at 3 GHz.

720

In Fig. 14 (a-d), the statistical variability of the mean retrieved PSD using a single-frequency shows good overlap within interpercentile ranges, except for panel (d) where occurrences for particle sizes between several hundred and several thousand  $\mu\text{m}$  are overestimated. Table 3 shows that the estimated mean IWC for this temperature bin is about three times larger than the in-situ value. This table also shows that the mean estimated IWCs agree well with the in-situ mean values between the temperatures of -50 to -20°C.

725

**Table 3** Comparison of retrieved (Ret) and in-situ (In) statistics for the mean and standard deviation of the IWC in each temperature bin, with the total number (num) of retrievals and measurements filtered into each temperature bin.

Temp Bin (°C)	In-situ num	Ret num	$Ret \overline{IWC} \pm \sigma$ ( $\text{g m}^{-3}$ )	$In \overline{IWC} \pm \sigma$ ( $\text{g m}^{-3}$ )
-50 to -40	137	35	0.015±0.003	0.014±0.008
-40 to -30	285	88	0.023±0.009	0.021±0.005
-30 to -20	510	135	0.034±0.019	0.030±0.011
-20 to -10	31	11	0.040±0.013	0.013±0.007

730 Critically, the single-frequency retrievals agree well with the in-situ measured IWCs across the sampled temperature range. For this case, the differences between the forward-modelled radar reflectivities at 35 GHz and the observations when using the retrieved PSDs and scattering model are like those already presented for C374 in Fig. 11, and so are not repeated here for reasons of brevity. Suffice to say that generally throughout the cloud layer, between about 5.5 and 8 km, the measurement residuals are generally  $\ll 0.5$  dBZ for all overpass times. Having studied C374 and C379, we now examine the final case  
735 C382.

### 5.3 The case C382

Case C382 represents a test of the retrieval methodology for ice clouds that are geometrically thinner than the other two cases. To avoid precipitation contamination of approximately just over 1 mm/hr between 16.00 and 17.00 hours, this analysis focusses on the radar profile at 15.117 hours, allowing application of the full dual-frequency retrieval methodology to the 3, 35 and 94  
740 GHz radar profiles. For this case, the in-situ sampling began at 16.55 and continued until about 17.15 hours, some 60–90 minutes after the first figure-of-eight overpasses, which began at about 15.00 and ended at 15.43 hours.

#### 5.3.1 Moment estimations and comparisons with aircraft data for C382

Following the established methodology, we first examine the ML performance in predicting the PSD moments used in the dual-frequency retrievals. The IWC profile is retrieved at 3 GHz assuming the exponential size distribution function. Figure  
745 15 (a–d), reveals a failure of the ML model for this thinner and colder ice cloud case, with minimal overlap between predicted and observed distributions. The ML-predicted  $D_{\text{mmw}}$  peaks at approximately 470  $\mu\text{m}$  compared to the in-situ peak near to 600  $\mu\text{m}$ . The higher-order moments show even larger systematic underestimation, with predicted distribution shapes differing significantly from the in-situ distributions.

This ML failure likely occurs because C382 falls outside the model's training domain. The PICASSO campaign training  
750 dataset predominantly sampled lower-altitude warmer ice clouds. This underscores the importance of ensuring training datasets encompass the full range of atmospheric conditions expected in applications. This is also why the ML PSD profiles are generally used as the first guess estimates to aid physics-based multi-frequency radar retrievals of the PSDs.

755

760

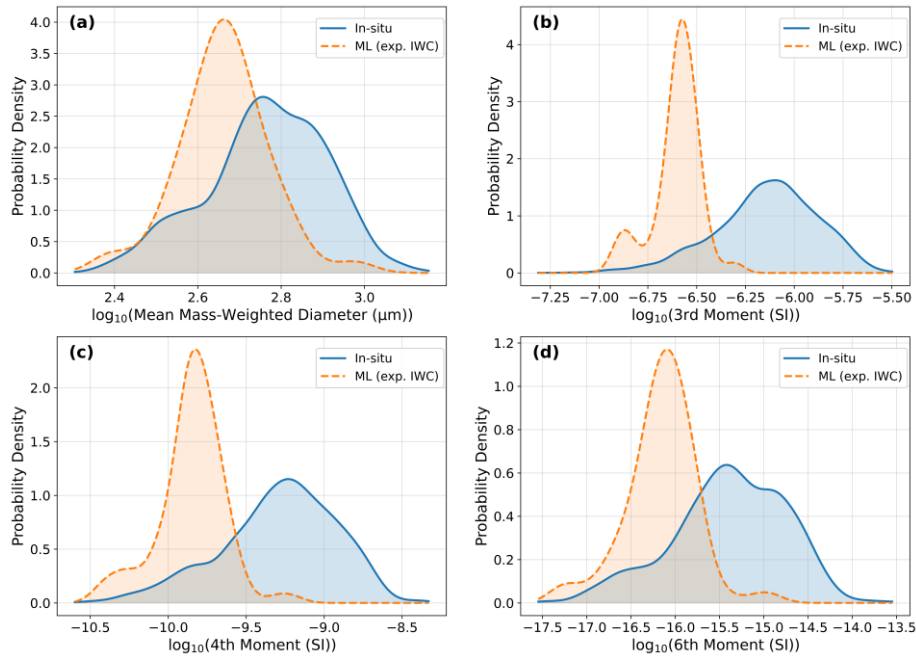


**Figure 15** As Fig. 13, but for C382.

### 5.3.2 Dual-frequency retrievals of the PSDs and comparisons with the in-situ composite PSDs for C382

765 Using the dual-frequency retrieval method with the ML-predicted moments from Fig. 15, the retrieved PSDs are compared with the in-situ measurements as a function of in-cloud temperature in Fig. 16 (a–c), following the same procedures as the other cases. Results assume the exp size distribution for the retrieval of IWC at 3 GHz for altitudes greater than 5 km and IWCs greater than  $0.002 \text{ g m}^{-3}$ . The ice cloud was situated between approximately 5.0 and 8 km, with the in-cloud temperatures stratified into three in-cloud temperature bins:  $-50$  to  $-40^\circ\text{C}$ ,  $-40$  to  $-30^\circ\text{C}$ , and  $-30$  to  $-20^\circ\text{C}$ .

770 Figure 16 (a–c) reveals that the dual-frequency retrievals do not improve upon the first-guess profiles, with mean retrieved PSDs generally systematically underestimating the in-situ number concentrations across all particle sizes at the two coldest temperature bins and for sizes greater than several hundred microns at the warmest temperature bin. This systematic bias propagates to substantial underestimation of computed IWC by several factors (not shown here for reasons of brevity). The in-situ PSDs exhibit notably broad distributions even at the coldest temperatures, suggesting the presence of large ice crystals

775 throughout the sample volume of the in-situ measurements. Moreover, changing to the gamma size distribution to retrieve the IWC at 3 GHz does not fundamentally alter these results, indicating that the mismatch between ML predictions and the ice cloud conditions cannot be bridged by PSD parameter optimisation alone.

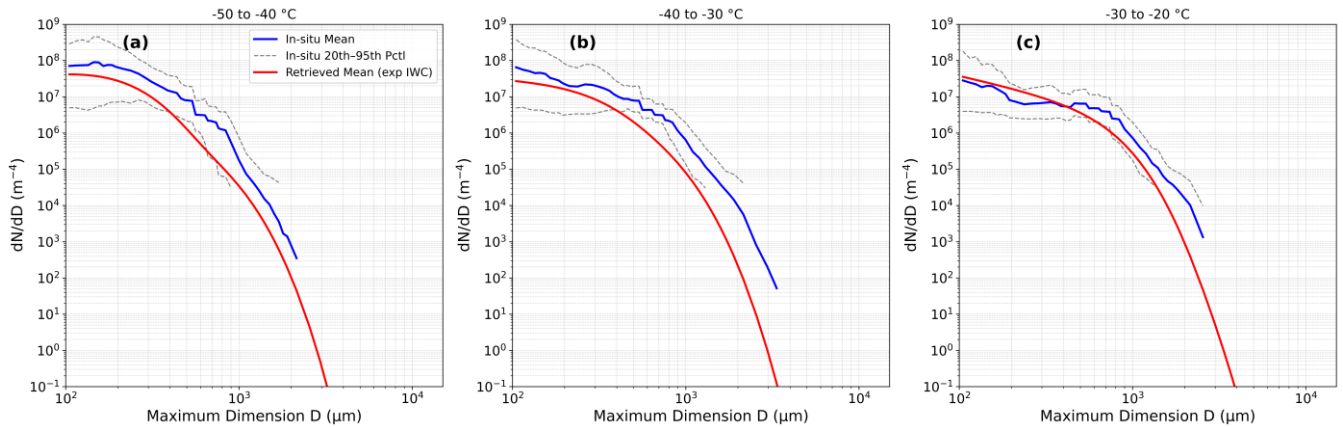


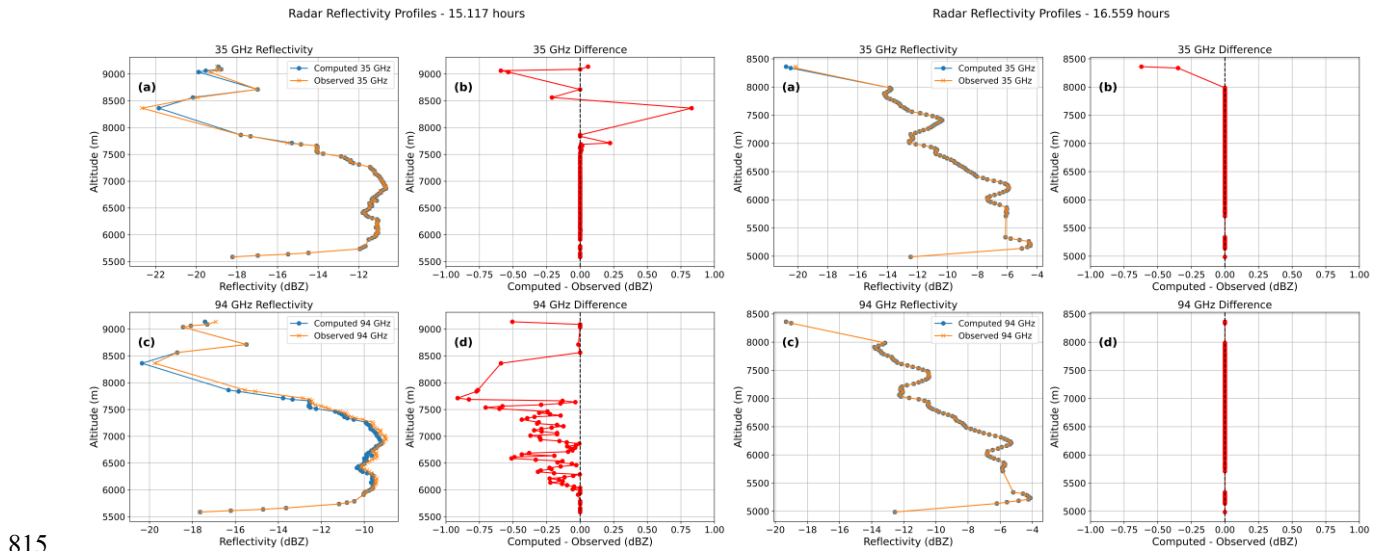
**Figure 16** As Fig. 14 but for C382 and temperature bins of (a) -50 to -40°C, (b) -40 to -30°C, and (c) -30 to -20°C.

785 To investigate whether improved initial conditions could enhance performance, we replaced the ML model predictions with the in-situ derived gamma PSD parameters as the first guess estimates. The results of this investigation revealed that this substitution does not improve agreement between the retrieved and in-situ PSDs, the results being very similar to Fig. 16 and so are not reproduced here for reasons of brevity. Despite starting from nearly perfect conditions, the dual-frequency optimisation consistently drives the retrievals away from the in-situ measurements. This systematic divergence may suggest  
790 that the fundamental issue lies with a mismatch between the radar observations and the in-situ measurements themselves, most likely owing to temporal evolution of the ice cloud between radar sampling, which began at 15.117 hrs and ended at 16.559 hrs, and the later in-situ aircraft measurements. The 90-minute interval between the beginning radar sampling time and the in-situ sampling that started after 16.559 hrs allowed the cloud to evolve toward broader PSDs with larger ice crystals.

To test whether the assumed Cotton et al. (2013) mass–dimension relation used in the rosette-aggregate scattering model is  
795 consistent with the in-situ measurements for C382, the IWC was re-computed from the composite PSDs using the relation in Eq. (10) and compared with the IWC derived from the Nevzorov probe. The re-computed PSD IWCs show a strong correlation with the measured IWCs with the correlation coefficient,  $r=0.88$ , and root mean square error of  $0.014 \text{ g m}^{-3}$ , and bias of  $-0.006 \text{ g m}^{-3}$ . The very good agreement obtained between the re-computed IWCs and the measured IWCs indicates that the assumed mass–dimension used for the rosette-aggregate scattering model is consistent with the in-situ IWC and cannot explain the  
800 discrepancy between the retrieved and in-situ PSDs.

Figure 17 presents the measurement residual analysis for the dual-frequency radar retrievals at the beginning of the radar sampling time at 15.117 hrs (left panel) and at the end time 16.559 hrs (right panel). The 35 GHz residuals at 15.117 hrs are quite stable, with most retrieval residuals being well within  $\pm 0.25 \text{ dBZ}$ . At 94 GHz, the residuals demonstrate a systematic negative bias in the presence of very small residuals at the corresponding 35 GHz altitudes, though most residuals are between

805 zero and -0.5 dBZ. This asymmetry in the residual analysis is a result of the retrieval optimisation favouring the 35 GHz match at the expense of the 94 GHz match, which suggests that at the beginning of the radar sampling the scattering model might not be completely representative of ice habits at this time. However, both frequency residuals at the time of 16.559 hrs are essentially zero, except for near the cloud top at 35 GHz, and inspection of the other six radar-sampling times shows that the 94 GHz residual structure becomes progressively less noisy from beginning to end. The progressive stabilisation of the 94 GHz residual structure possibly suggests that the cloud evolves to ice habits that are more consistent with the scattering model used here, future radiative transfer studies will study this aspect further. Given the evolution of the 94 GHz residuals that is represented by Fig. 17, the temporal-evolution hypothesis remains the most plausible explanation for the discrepancy between the in-situ and retrieved PSDs.



815

**Figure 17** Same as Fig. 11, but for the case C382 at the time of 15.117 hrs (left panel) and 15.559 hrs (right panel). Effects of a thin cirrus layer detached from the main ice layer can be seen at altitudes between about 8.5 and 9 km (left panel).

## 6 Summary and conclusions

820 In this paper, a new retrieval methodology has been presented for estimating mid-latitude PSD parameters using multi-frequency radar observations. The approach combines ensemble machine learning predictions of  $M_2$ ,  $M_3$ ,  $M_4$ , and  $M_6$  moments of the PSD with dual-frequency optimised physical retrievals based on the randomly oriented rosette aggregate ice crystal scattering model. The ensemble ML model, trained on the PICASSO climatology, provides robust first guess profiles of the PSD parameters  $N_0$ ,  $\lambda$  and  $\mu$ , where  $N_0$  and  $\lambda$  are subsequently refined by the physical retrieval to achieve simultaneous

825 agreement with the 35 and 94 GHz radar reflectivities. The 3 GHz radar data are used separately to retrieve the IWC profiles that enter the ML feature vector to ultimately inform the retrieval of the PSDs.

Application of this retrieval methodology to three of the CCREST-M case studies (i.e., C374, C379 and C382), supported by the FAAM aircraft in-situ measurements, demonstrates that for the combined ML–physics methodology yields PSDs that reproduce observed radar reflectivities to within typically  $\pm 0.25 - 0.5$  dBZ for well-constrained cases such as C374. Comparisons with in-situ composite PSDs show that the retrievals capture the observed variability as a function of temperature, with generally good agreement in mean values of the number concentration with ice crystal maximum dimension. The choice of PSD functional form (i.e., the exponential or gamma size distributions) also introduces some sensitivity when retrieving the IWC using the 3 GHz radar profiles. For the case C374, the gamma size distribution assumption is largely within the interpercentile ranges of the in-situ PSDs and the estimated IWCs are statistically within the ranges of the in-situ measured IWC. The exponential size distribution could overestimate the number concentrations at the smaller and larger sizes, though were also largely within the in-situ ranges of the measured IWCs, apart from the warmest temperature bin. Independent validation with the 200 GHz radar reflectivities confirms the applicability of the rosette aggregate ice crystal scattering model for the bulk of the ice cloud above approximately 4.5 km, where the rosette aggregates were the predominant in-situ habit. In the lower cloud regions, the presence of other ice particle types was the likely cause of departures of the rosette aggregate model simulations from the measurements. The 200 GHz validation could not distinguish between the two PSD assumptions, and so no one PSD assumption was found to be the better choice.

For C379, the 35 GHz single-frequency retrievals of the PSDs achieved successful PSD retrievals when the ML first guess was also very good. However, the retrieved PSDs using the physically based optimisation method improved the ML first guess estimates and agreed well with the in-situ measurements for most of the temperature bins, demonstrating that single-frequency optimisation can still refine physically realistic first guess profiles when the ML model estimate is good.

However, for the case C382, limitations of the retrieval methodology were evident, where the presented methodology degrades in colder, thinner clouds where ML predictions extrapolate beyond their training range. For instance, in the case of C374 and C379, the ML first guess normalised distributions of the moments were found to overlap well with the normalised distributions of the in-situ derived moments. Only in the case of C382 did the ML method fail owing to an extrapolation being required rather than an interpolation. Case-to-case differences emphasise the need for diverse training datasets and capturing the temporal evolution of ice clouds for multi-frequency approaches to robustly characterise ice cloud microphysics. For C382, the optimised retrieval did produce converged retrievals with 35 GHz residuals essentially being at zero for most of the cloud layer during the radar-sampling period. However, the 94 GHz residuals revealed a small systematic negative bias at the beginning of the radar sampling but diminished and became essentially zero by the end of the sampling period. The 90-minute time difference between the beginning of the radar sampling and in-situ sampling, combined with the evolution noted in the 94 GHz measurement residuals, strongly supports temporal evolution as the primary cause of the in-situ versus retrieved PSD disagreement.

A paper in preparation will use the same rosette aggregate ice crystal scattering model, together with the retrieved PSDs for all three cases, to forward model radiative transfer simulations of brightness temperatures across the mm-wave and sub-mm-wave spectrum. This will allow us to assess the consistency between the radar-constrained retrievals and the suitability of the adopted scattering model, using collocated radiometer measurements, for forward modelling in the data assimilation process.

## References

- Abel, S. J., Cotton, R. J., Barrett, P. A., and Vance, A. K.: A comparison of ice water content measurement techniques on the FAAM BAe-146 aircraft, *Atmos. Meas. Tech.*, 7, 3007–3022, <https://doi.org/10.5194/amt-7-3007-2014>, 2014.
- Atlas, D., Matrosov, S. Y., Heymsfield, A. J., Chou, M., and Wolff, D. B.: Radar and Radiation Properties of Ice Clouds. *J. Appl. Meteor. Climatol.*, 34, 2329–2345, [https://doi.org/10.1175/1520-0450\(1995\)034<2329:RARPOI>2.0.CO;2](https://doi.org/10.1175/1520-0450(1995)034<2329:RARPOI>2.0.CO;2), 1995.
- Baran, A. J., Heymsfield, A. J., Kleanthous, A., Westbrook, C. D., Betcke, T., Hewett, D. P., Barrett, P., and Fox, S.: Testing the Consistency of the Boundary Element Method for Computing the Backscattering Properties of Complex Ice Crystals at Multiple Radar Frequencies. In *IGARSS 2024-2024 IEEE International Geoscience and Remote Sensing Symposium*, 538-541, IEEE, 2024.
- Baran, A. J.: From the single-scattering properties of ice crystals to climate prediction: A way forward. *Atmos. Res.*, 112, 45-69, <https://doi.org/10.1016/j.atmosres.2012.04.010>, 2012.
- Baran, A.J., Bodas-Salcedo, A., Cotton, R., Lee, C.: Simulating the equivalent radar reflectivity of cirrus at 94 GHz using an ensemble model of cirrus ice crystals: a test of the Met Office global numerical weather prediction model. *Q.J.R. Meteorol. Soc.*, 137: 1547-1560. <https://doi.org/10.1002/qj.870>, 2011.
- Baran, A. J.: A review of the light scattering properties of cirrus, *J. Quant. Spectrosc. Ra.*, 110, 1239–1260, <https://doi.org/10.1016/j.jqsrt.2009.02.026>, 2009.
- Barker, H. W., Cole, J. N. S., Villefranque, N., Qu, Z., Velázquez Blázquez, A., Domenech, C., Mason, S. L., and Hogan, R. J.: Radiative closure assessment of retrieved cloud and aerosol properties for the EarthCARE mission: the ACMB-DF product, *Atmos. Meas. Tech.*, 18, 3095–3107, <https://doi.org/10.5194/amt-18-3095-2025>, 2025.
- Bartolomé García, I., Sourdeval, O., Spang, R., and Krämer, M.: Technical note: Bimodal parameterizations of in situ ice cloud particle size distributions, *Atmos. Chem. Phys.*, 24, 1699–1716, <https://doi.org/10.5194/acp-24-1699-2024>, 2024.
- Brath, M., Ekelund, R., Eriksson, P., Lemke, O., and Buehler, S. A.: Microwave and submillimeter wave scattering of oriented ice particles, *Atmos. Meas. Tech.*, 13, 2309–2333, <https://doi.org/10.5194/amt-13-2309-2020>, 2020.
- Cotton, R.J., Field, P.R., Ulanowski, Z., Kaye, P.H., Hirst, E., Greenaway, R.S., Crawford, I., Crosier, J., Dorsey, J.: The effective density of small ice particles obtained from in situ aircraft observations of mid-latitude cirrus. *Q.J.R. Meteorol. Soc.*, 139, 1923-1934. <https://doi.org/10.1002/qj.2058>, 2013.
- Courtier, B. M., Battaglia, A., Huggard, P. G., Westbrook, C., Mroz, K., Dhillon, R. S., et al.: First observations of G-band radar Doppler spectra. *Geophys. Res. Lett.*, 49, e2021GL096475. <https://doi.org/10.1029/2021GL096475>, 2022.
- Delanoë, J., et al.: BASTA: A 95-GHz FMCW Doppler Radar for Cloud and Fog Studies. *J. Atmos. Oceanic Technol.*, 33, 1023–1038, <https://doi.org/10.1175/JTECH-D-15-0104.1>, 2016.

- 905 Duffy, G., and D. J. Posselt.: A Gamma Parameterization for Precipitating Particle Size Distributions Containing Snowflake  
Aggregates Drawn from Five Field Experiments. *J. Appl. Meteor. Climatol.*, 61, 1077–1085, <https://doi.org/10.1175/JAMC-D-21-0131.1>, 2022.
- 910 Ellison, W.J.: Permittivity of pure water, at standard atmospheric pressure, over the frequency range 0-25  
THz and the temperature range 0-100°C. *J. Phys. Chem. Ref. Data*, 36, doi:10.1063/1.2360986, 2007.
- Eriksson, P., Rydberg, B., Mattioli, V., Thoss, A., Accadia, C., Klein, U., and Buehler, S. A.: Towards an operational Ice  
Cloud Imager (ICI) retrieval product, *Atmos. Meas. Tech.*, 13, 53–71, <https://doi.org/10.5194/amt-13-53-2020>, 2020.
- 915 Eriksson, P., Ekelund, R., Mendrok, J., Brath, M., Lemke, O., and Buehler, S. A.: A general database of hydrometeor single  
scattering properties at microwave and sub-millimetre wavelengths, *Earth Syst. Sci. Data*, 10, 1301–1326,  
<https://doi.org/10.5194/essd-10-1301-2018>, 2018.
- 920 Field, P.R., Hill, A., Shipway, B., Furtado, K., Wilkinson, J., Miltenberger, A., et al.: Implementation of a double moment  
cloud microphysics scheme in the UK met office regional numerical weather prediction model. *Q.J.R. Meteorol. Soc.*, 149,  
703–739. Available from: <https://doi.org/10.1002/qj.4414>, 2023.
- Fontaine, E., Leroy, D., Schwarzenboeck, A., Delanoë, J., Protat, A., Dezitter, F., Grandin, A., Strapp, J. W., and Lilie, L. E.:  
Evaluation of radar reflectivity factor simulations of ice crystal populations from in situ observations for the retrieval of  
condensed water content in tropical mesoscale convective systems, *Atmos. Meas. Tech.*, 10, 2239–2252,  
925 <https://doi.org/10.5194/amt-10-2239-2017>, 2017.
- Fox, S., Lee, C., Moyna, B., Philipp, M., Rule, I., Rogers, S., King, R., Oldfield, M., Rea, S., Henry, M., Wang, H., and  
Harlow, R. C.: ISMAR: an airborne submillimetre radiometer, *Atmos. Meas. Tech.*, 10, 477–490,  
<https://doi.org/10.5194/amt-10-477-2017>, 2017.
- 930 Geer, A. J., Bauer, P., Lonitz, K., Barlakas, V., Eriksson, P., Mendrok, J., Doherty, A., Hocking, J., and Chambon, P.: Bulk  
hydrometeor optical properties for microwave and sub-millimetre radiative transfer in RTTOV-SCATT v13.0, *Geosci.  
Model Dev.*, 14, 7497–7526, <https://doi.org/10.5194/gmd-14-7497-2021>, 2021.
- 935 Geer, A. J., Baordo, F., Bormann, N., English, S., Kazumori, M., Lawrence, H., Lean, P., Lonitz, K., and Lupu, C.: The  
growing impact of satellite observations sensitive to humidity, cloud and precipitation, *Q. J. Roy. Meteor. Soc.*, 143, 3189–  
3206, <https://doi.org/10.1002/qj.3172>, 2017.
- 940 Geer, A. J., Baordo, F.: Improved scattering radiative transfer for frozen hydrometeors at microwave frequencies. *Atmos.  
Meas. Tech.*, 7, 1839–1860, <https://doi.org/10.5194/amt-7-1839-2014>, 2014.
- 945 Heymsfield, A., Bansemer, A., Heymsfield, G., Noone, D., Grecu, M., Toohey, D.: Relationship of Multiwavelength Radar  
Measurements to Ice Microphysics from the IMPACTS Field Program. *J. Appl. Meteor. Climatol.*, 62, 289–315,  
<https://doi.org/10.1175/JAMC-D-22-0057.1>, 2023.
- Hogan, R. J., Mittermaier, M. P., Illingworth, A. J.: The retrieval of ice water content from radar reflectivity factor and  
temperature and its use in evaluating a mesoscale model. *J. Appl. Meteor. Climatol.*, 45, 301–317.,  
<https://doi.org/10.1175/JAM2340.1>, 2006.
- 950 Hogan, R. J., Illingworth, A. J., Sauvageot, H.: Measuring Crystal Size in Cirrus Using 35- and 94-GHz Radars. *J. Atmos.  
Oceanic Technol.*, 17, 27–37, [https://doi.org/10.1175/1520-0426\(2000\)017<0027:MCSICU>2.0.CO;2](https://doi.org/10.1175/1520-0426(2000)017<0027:MCSICU>2.0.CO;2), 2000.

- 955 Hong, G., Yang, P., Baum, B. A., and Heymsfield, A. J.: Relationship between ice water content and equivalent radar reflectivity for clouds consisting of nonspherical ice particles, *J. Geophys. Res.*, 113, D20205, doi:[10.1029/2008JD009890](https://doi.org/10.1029/2008JD009890), 2008.
- Hong, Y., Meng, H., Fan, Y., Dong, J., Ren, T., and Yang, P.: The effects of ice habit models on passive snowfall rate retrievals. *Geophys. Res. Lett.*, 52, e2025GL11685, <https://doi.org/10.1029/2025GL116853>, 2025.
- 960 Illingworth, A. J. et al.: The EarthCARE Satellite: The Next Step Forward in Global Measurements of Clouds, Aerosols, Precipitation, and Radiation. *Bull. Amer. Meteor. Soc.*, 96, 1311–1332, <https://doi.org/10.1175/BAMS-D-12-00227.1>, 2015.
- International Telecommunication Union (ITU). P.676 : Attenuation by atmospheric gases and related effects. 2022. ITU. Available at: <https://www.itu.int/rec/R-REC-P.676-13-202208-I/en>
- 965 Janisková., M.: Assimilation of cloud information from space-borne radar and lidar: experimental study using a 1D+4D-Var technique. *Q.J.R. Meteorol. Soc.*, 141: 2708-2725. <https://doi.org/10.1002/qj.2558>, 2015.
- 970 Kleanthous, A., Baran, A. J., Betcke, T., Hewett, D. P., and Westbrook, C. D.: An application of the boundary element method (BEM) to the calculation of the single-scattering properties of very complex ice crystals in the microwave and sub-millimetre regions of the electromagnetic spectrum, *J. Quant. Spectrosc. Radiat. Transf.*, 312, 108793, <https://doi.org/10.1016/j.jqsrt.2023.108793>, 2024.
- 975 Kleanthous, A., Betcke, T., Hewett, D. P., Escapil-Inchauspé, P., Jerez-Hanckes, C., and Baran, A. J.: Accelerated Calderón preconditioning for Maxwell transmission problems, *J. Comput. Phys.*, 458, 111099, <https://doi.org/10.1016/j.jcp.2022.111099>, 2022.
- 980 Kozu, T., and Nakamura, K.: Rainfall Parameter Estimation from Dual-Radar Measurements Combining Reflectivity Profile and Path-integrated Attenuation. *J. Atmos. Oceanic Technol.*, 8, 259–270, [https://doi.org/10.1175/1520-0426\(1991\)008<0259:RPEFDR>2.0.CO;2](https://doi.org/10.1175/1520-0426(1991)008<0259:RPEFDR>2.0.CO;2), 1991.
- Krämer, M., Spelten, N., Rolf, C., and Spang, R.: A microphysics guide to cirrus – Part 3: Occurrence patterns of cloud particles, *Atmos. Chem. Phys.*, 25, 13563–13583, <https://doi.org/10.5194/acp-25-13563-2025>, 2025.
- 985 Lawson, R. P., Woods, S., Jensen, E., Erfani, E., Gurganus, C., Gallagher, M., et al.: A review of ice particle shapes in cirrus formed in situ and in anvils. *J. Geophys. Res.: Atmos.*, 124, 10049–10090. <https://doi.org/10.1029/2018JD030122>, 2019.
- 990 Li, Q., Li, H., Sun, X., Zhang, Y., Lyu, W., Ruan, Z., Liu, L., Liu, A., and Zhang, C.: A survey of snow growth signatures from tropics to Antarctica using triple-frequency radar observations, *Atmos. Chem. Phys.*, 26, 1249–1264, <https://doi.org/10.5194/acp-26-1249-2026>, 2026.
- 995 Liu, P., Gao, J., Zhang, G., Carlin, J. T.: Assimilation of radar reflectivity data using parameterized forward operators for improving short-term forecasts of high-impact convection events. *Journal of Geophysical Research: Atmospheres*, 129, e2024JD041458. <https://doi.org/10.1029/2024JD041458>, 2024.
- Liou, K.: Influence of Cirrus Clouds on Weather and Climate Processes: A Global Perspective. *Mon. Wea. Rev.*, 114, 1167–1199, [https://doi.org/10.1175/1520-0493\(1986\)114<1167:IOCCOW>2.0.CO;2](https://doi.org/10.1175/1520-0493(1986)114<1167:IOCCOW>2.0.CO;2), 1986.
- 1000 Liou, K. N. and Yang, P.: *Light Scattering by Ice Crystals: fundamentals and applications*, Cambridge University Press, Cambridge, UK, 2016.

- Mätzler, C., Rosenkranz, P., Battaglia, A., Wigneron, J.: Microwave dielectric properties of ice. *Thermal microwave radiation: applications for remote sensing*, 52, 455-462, 2006.
- 1005 Mason, S. L., Barker, H. W., Cole, J. N. S., Docter, N., Donovan, D. P., Hogan, R. J., Hünerbein, A., Kollias, P., Puigdomènech Treserras, B., Qu, Z., Wandinger, U., and van Zadelhoff, G.-J.: An intercomparison of EarthCARE cloud, aerosol, and precipitation retrieval products, *Atmos. Meas. Tech.*, 17, 875–898, <https://doi.org/10.5194/amt-17-875-2024>, 2024.
- 1010 May, E., Rydberg, B., Kaur, I., Mattioli, V., Hallborn, H., and Eriksson, P.: The Ice Cloud Imager: retrieval of frozen water column properties, *Atmos. Meas. Tech.*, 17, 5957–5987, <https://doi.org/10.5194/amt-17-5957-2024>, 2024.
- 1015 McCusker, K., Westbrook, C., Battaglia, A., Mroz, K., Courtier, B. M., Huggard, P. G., Wang, H., Reeves, R., Walden, C. J., Cotton, R., Fox, S., and Baran, A. J.: Estimating vertical profiles of ice water content and snowfall rate from radar measurements in the G-band, *Atmos. Meas. Tech.*, 18, 7833–7852, <https://doi.org/10.5194/amt-18-7833-2025>, 2025.
- 1020 McCusker, K., Baran, A. J., Westbrook, C., Fox, S., Eriksson, P., Cotton, R., Delanoë, J., and Ewald, F.: The first microwave and submillimetre closure study using particle models of oriented ice hydrometeors to simulate polarimetric measurements of ice clouds. *Atmos. Meas. Tech.*, 17, 3533-3552, <https://amt.copernicus.org/articles/17/3533/2024/amt-17-3533-2024.html>, 2024.
- 1025 McFarquhar, G. M., Baumgardner, D., Bansemmer, A., Abel, S. J., Crosier, J., French, J., Rosenberg, P., Korolev, A., Schwarzen-Boeck, A., Leroy, D., Um, J., Wu, W., Heymsfield, A. J., Twohy, C., Detwiler, A., Field, P., Neumann, A., Cotton, R., Axisa, D., and Dong, J.: Processing of Ice Cloud In Situ Data Collected by Bulk Water, Scattering, and Imaging Probes: Fundamentals, Uncertainties, and Efforts toward Consistency, *Meteor. Mon.*, 58, 11.1–11.33, <https://doi.org/10.1175/AMSMONOGRAPHS-D-16-0007.1>, 2017.
- 1030 Naud, C. M., J. Muller, E. C. Slack, C. L. Wrench, and E. E. Clothiaux.: Assessment of the Performance of the Chilbolton 3-GHz Advanced Meteorological Radar for Cloud-Top-Height Retrieval. *J. Appl. Meteor. Climatol.*, 44, 876–887, <https://doi.org/10.1175/JAM2244.1>, 2005.
- Nelder, J. A., Mead, R. A Simplex Method for Function Minimization, *The Computer Journal*, 7, Issue 4, Pages 308–313, <https://doi.org/10.1093/comjnl/7.4.308>, 1965.
- 1035 Pedregosa, F., Varoquaux, G., Gramfort, A., Michel, V., Thirion, B., Grisel, O., Blondel, M., et al. Scikit-learn: Machine learning in Python. *Journal of machine Learning research*, 12, 2825-2830, [https://www.jmlr.org/papers/volume12/pedregosa11a/pedregosa11a.pdf?source=post\\_page](https://www.jmlr.org/papers/volume12/pedregosa11a/pedregosa11a.pdf?source=post_page), 2011.
- 1040 Schrom, R. S., Kumjian, M. R.: A Probabilistic Radar Forward Model for Branched Planar Ice Crystals. *J. Appl. Meteor. Climatol.*, 58, 1245–1265, <https://doi.org/10.1175/JAMC-D-18-0204.1>, 2019.
- 1045 Sephton, E.: Understanding the Origins of Ice in Mixed-Phase Layer Clouds (Doctoral dissertation, The University of Manchester (United Kingdom)), <https://search.proquest.com/openview/6bd6e902c7690c8413a32a3734738137/1?pq-origsite=gscholar&cbl=2026366&diss=y>, 2022.
- Wagner, S. W., Schnaiter, M., Xu, G., Rogge, F., and Järvinen, E.: Light scattering and microphysical properties of atmospheric bullet rosette ice crystals, *Atmos. Chem. Phys.*, 25, 8785–8804, <https://doi.org/10.5194/acp-25-8785-2025>, 2025.
- 1050 Walden, C.: UL HATPRO-G5. ACTRIS Cloud remote sensing data centre unit (CLU). <https://hdl.handle.net/21.12132/3.5f5640d6deb6491d>, 2026a.

Walden, C.: UKRI CL51. ACTRIS Cloud remote sensing data centre unit (CLU).  
<https://hdl.handle.net/21.12132/3.1ca2b7d6323f486b>, 2026b.

1055

Wang, S. and Liu, Z.: A radar reflectivity operator with ice-phase hydrometeors for variational data assimilation (version 1.0) and its evaluation with real radar data, *Geosci. Model Dev.*, 12, 4031–4051, <https://doi.org/10.5194/gmd-12-4031-2019>, 2019.

1060

Westbrook, C.D., Ball, R.C., Field, P.R. and Heymsfield, A.J.: A theory of growth by differential sedimentation with application to snowflake formation. *Physical Review E*, 70, <https://doi.org/10.1103/PhysRevE.70.021403>, 2004.

Wood, N. B., L'Ecuyer, T. S.: What millimeter-wavelength radar reflectivity reveals about snowfall: an information-centric analysis, *Atmos. Meas. Tech.*, 14, 869–888, <https://doi.org/10.5194/amt-14-869-2021>, 2021.

1065

Wu, B., Wang, Y., Fan, X., Liu, S., and Fu, Y.: A mixing scheme of ice particle models for global ice cloud measurements. *Remote Sensing of Environment*, 313, 114356, <https://doi.org/10.1016/j.rse.2024.114356>, 2024.

Yang, P., Liou, KN., Bi, L. et al.: On the radiative properties of ice clouds: Light scattering, remote sensing, and radiation parameterization. *Adv. Atmos. Sci.* 32, 32–63, <https://doi.org/10.1007/s00376-014-0011-z>, 2015.

1070

## Supplement

### Code availability

1075

CCREST-M code is available upon request.

### Data availability

1080

The CCREST-M dropsonde, and aircraft in-situ measurements and the 3 (CAMRa), and 35 GHz (Kepler) radar data are available from the CEDA website located here: <https://archive.ceda.ac.uk/>

### Author contribution

1085

AJB conceived the scientific objectives of the CCREST-M campaign, developed the retrieval methodology and its implementation, performed the retrieval and in-situ comparison analyses, and led the writing of the manuscript, including revisions. SF co-developed the scientific aims of the CCREST-M campaign, served as the principal lead for the aircraft flight operations, provided the atmospheric and radar datasets for the retrievals, and contributed to the manuscript review and preparation for submission. RC provided the in-situ PSD and Nevzorov data analyses, supplied the PICASSO PSD

1090

climatology, and contributed to manuscript proofing. JD provided the 94 GHz mini-BASTA radar data and its processing and contributed to manuscript proofing. CJW operated the Chilbolton Observatory radars during the CCREST-M campaign, provided and processed the CAMRa (3 GHz) and Kepler (35 GHz) radar datasets, and assisted with manuscript proofing. KM supplied the 200 GHz radar data and applied the necessary corrections for ice crystals, liquid water, and atmospheric

1095

attenuation. CDW provided the C081 PICASSO 3 GHz data, corrections for the near-antenna 3 GHz CCREST-M data, 200 GHz processed data, and assisted with manuscript proofing. PGH and the GRaCE team operated the 200 GHz radar system, provided the datasets to KM and CDW and contributed to manuscript proofing.

### Competing interests

1100

The authors declare that they have no conflict of interest.

## **Acknowledgements**

The authors would like to thank the crew and personnel involved in the CCREST-M campaign and the Chilbolton Observatory and mini-BASTA radar operators, and the personnel involved in the operation of the 200 GHz radar at Chilbolton Observatory. 1105 The BAe-146 research aircraft is operated by Airtask and Avalon and managed by FAAM. We further thank NCAS for the availability of the 35 GHz radar and CNRS, and the LATMOS for providing, operating, and delivering to the Chilbolton Observatory the mini-BASTA radar. Access to the 3 and 35 GHz radars was provided through the Atmospheric Measurement and Observation Facility (AMOF), part of UKRI-NERC funded National Capability delivered by the National Centre for Atmospheric Science (NCAS).